Monthly Notices
of the
ROYAL ASTRONOMICAL SOCIETY

MNRAS **483,** 806–823 (2019)
Advance Access publication 2018 November 16

doi:10.1093/mnras/sty3078

First ALMA maps of HCO, an important precursor of complex organic molecules, towards IRAS 16293–2422

V. M. Rivilla,[1]★ M. T. Beltrán,[1] A. Vasyunin,[2,3,4] P. Caselli,[2] S. Viti,[5] F. Fontani[1] and R. Cesaroni[1]

[1]*INAF-Osservatorio Astrofisico di Arcetri, Largo Enrico Fermi 5, I-50125 Florence, Italy*
[2]*Max-Planck-Institute for Extraterrestrial Physics, Garching D-85748, Germany*
[3]*Ural Federal University, Ekaterinburg 620002, Russia*
[4]*Engineering Research Institute, 'Ventspils International Radio Astronomy Centre' of Ventspils University of Applied Sciences, Inženieru 101, Ventspils LV-3601, Latvia*
[5]*Department of Physics and Astronomy, University College London, Gower Street, London, WC1E 6BT, UK*

Accepted 2018 October 30. Received 2018 October 8; in original form 2018 May 16

ABSTRACT

The formyl radical HCO has been proposed as the basic precursor of many complex organic molecules such as methanol (CH_3OH) and glycolaldehyde (CH_2OHCHO). Using ALMA, we have mapped, for the first time at high angular resolution (∼1 arcsec, ∼140 au), HCO towards the solar-type protostellar binary IRAS 16293–2422, where numerous complex organic molecules have been previously detected. We also detected several lines of the chemically related species H_2CO, CH_3OH, and CH_2OHCHO. The observations revealed compact HCO emission arising from the two protostars. The line profiles also show redshifted absorption produced by foreground material of the circumbinary envelope that is infalling towards the protostars. Additionally, IRAM 30 m single-dish data revealed a more extended HCO component arising from the common circumbinary envelope. The comparison between the observed molecular abundances and our chemical model suggests that whereas the extended HCO from the envelope can be formed via gas-phase reactions during the cold collapse of the natal core, the HCO in the hot corinos surrounding the protostars is predominantly formed by the hydrogenation of CO on the surface of dust grains and subsequent thermal desorption during the protostellar phase. The derived abundance of HCO in the dust grains is high enough to produce efficiently more complex species such as H_2CO, CH_3OH, and CH_2OHCHO by surface chemistry. We found that the main formation route of CH_2OHCHO is the reaction between HCO and CH_2OH.

Key words: astrochemistry – line: identification – molecular data – stars: formation – stars: low-mass – ISM: molecules.

1 INTRODUCTION

The formation of complex organic molecules (COMs) – carbon-based compounds with more than five atoms (Herbst & van Dishoeck 2009) – is being intensively debated in astrochemistry. COMs play a central role in pre-biotic chemistry and may be directly linked to the origin of life (e.g. Caselli & Ceccarelli 2012). Numerous efforts have been made in the last years to understand how COMs are formed in the interstellar medium (ISM), by combining observations (e.g. Belloche et al. 2009; Jørgensen et al. 2016; Codella et al. 2017; Martín-Doménech et al. 2017; Rivilla et al. 2017a,b), chemical modelling (e.g. Garrod, Weaver & Herbst 2008; Vasyunin & Herbst 2013a,b; Balucani, Ceccarelli & Taquet 2015; Taquet, Wirström & Charnley 2016; Vasyunin et al. 2017; Bergantini et al. 2018; Coutens et al. 2018; Quénard et al. 2018a), and laboratory experiments (e.g. Fedoseev et al. 2015; Chuang et al. 2016, 2017). However, despite all the efforts, our understanding of the synthesis of COMs in the ISM is still very limited. Two general paradigms have been proposed: (i) gas-phase chemistry triggered by the evaporation (thermal or non-thermal) of interstellar ices (e.g. Millar et al. 1991; Vasyunin & Herbst 2013b; Balucani et al. 2015; Vasyunin et al. 2017) and (ii) hydrogenation and/or radical–radical reactions on dust grain surfaces (e.g. Garrod & Herbst 2006; Garrod et al. 2008).

A key step to understand how complex molecules are built up in the ISM is to study their molecular precursors, that is the basic pieces that lead to their formation. Many chemical models and laboratory

★ E-mail: rivilla@arcetri.astro.it

experiments have proposed that the simple formyl radical, HCO, is the precursor of COMs like methanol (Watanabe & Kouchi 2002), the sugar-like molecule glycolaldehyde and the sugar-alcohol ethylene glycol (Bennett & Kaiser 2007; Woods et al. 2012, 2013; Butscher et al. 2015; Fedoseev et al. 2015; Chuang et al. 2017), formamide (Jones, Bennett & Kaiser 2011, Fedoseev et al. 2016), and N-methylformamide (Belloche et al. 2017). However, despite the importance of HCO to build up chemical complexity, little is known so far about its formation itself. Two main scenarios have been proposed: (i) formation on the surface of dust grains via neutral−neutral reactions at cold starless stages (e.g. Tielens & Hagen 1982; Brown, Charnley & Millar 1988; Dartois et al. 1999; Watanabe & Kouchi 2002; Woon 2002; Garrod et al. 2008; Bacmann & Faure 2016) and (ii) formation via gas-phase chemistry (Bacmann & Faure 2016; Hickson et al. 2016).

To understand how HCO is formed, and what its role is in the formation of more complex species, dedicated observations of this molecule are needed. HCO has been detected in very different environments: diffuse clouds (Liszt et al. 2014), molecular clouds (Snyder, Hollis & Ulich 1976; Snyder, Schenewerk & Hollis 1985; Schenewerk, Snyder & Hjalmarson 1986; Schenewerk et al. 1988), photon-dominated regions (Schilke et al. 2001; Gerin et al. 2009), cold dark clouds (Cernicharo et al. 2012; Agúndez, Cernicharo & Guélin 2015), shocks (Jiménez-Serra et al. 2004), starless cores (Frau, Girart & Beltrán 2012; Bacmann & Faure 2016; Spezzano et al. 2017), low-mass protostellar objects (Caux et al. 2011; Bacmann & Faure 2016), and massive star-forming regions (Sánchez-Monge et al. 2013; Rivilla et al., in prep.). However, these observations have been carried out with single-dish telescopes, and hence, up to now, no high angular resolution observations of HCO are available. This has prevented us from revealing the HCO spatial distribution and properly deriving source-average abundances to be compared with chemical models.

IRAS 16293–2422 (hereafter IRAS16293) is a low-mass protostellar system located at a distance of 141^{+31}_{-21} pc (Dzib et al. 2018). It is composed of two solar-like protostars, sources A and B, surrounded by chemically rich hot corinos (Cazaux et al. 2003; Bottinelli et al. 2004) separated in the plane of the sky by ∼5 arcsec (∼705 au), and whose masses are ∼0.5 $M_\odot$ (Looney, Mundy & Welch 2000). Many COMs have been detected towards the two hot corinos of this system, including glycolaldehyde (CH_2OHCHO; Jørgensen et al. 2012), ethylene glycol [$(CH_2OH)_2$; Jørgensen et al. 2012], formamide (NH_2CHO; Kahane et al. 2013; Coutens et al. 2016), and methyl isocyanate (CH_3NCO; Ligterink et al. 2017; Martín-Doménech et al. 2017). The line profiles have linewidths of up to 8 km s^{-1} for A and <2 km s^{-1} for B, due to the different inclinations of the sources (B is almost face-on). Due to its chemical richness, IRAS16293 is an excellent laboratory for astrochemical studies.

In this paper, we present for the first time interferometric ALMA (Atacama Large Millimeter/Submillimeter Array) observations of HCO towards IRAS16293. We study the spatial distribution of this molecule and compare its molecular abundance with that of more complex species: H_2CO, CH_3OH, and CH_2OHCHO. We also present different chemical models to understand the formation of HCO itself, and its role in the formation of more complex species such as glycolaldehyde.

2 OBSERVATIONS

We carried out interferometric observations using 40 antennas of ALMA in Cycle 3 on 2016 June 11 as part of the project 2015.1.01193.S (PI Rivilla). The observations were performed in Band 3 (3 mm) with the array in a configuration with baselines ranging from 15 m to 783 m. The digital correlator was configured in four different spectral windows (SPWs) to cover lines of HCO, H_2CO, CH_3OH, and CH_2OHCHO. The precipitable water vapour (pwv) during the observations was in the range 2.0–2.4 mm. Flux calibration was obtained through observations of Titan. The phase was calibrated from interleaved observations of the quasar J1625–2527. The bandpass correction was obtained by observing the BL Lacertae object J1517–2422. The on-source observing time was about 70 min. The phase centre was RA = $16^h32^m22\overset{s}{.}62$, Dec. = $-24°28'32\overset{''}{.}46$.

Table 1. ALMA observations used in this work.

SPW	Frequency range (GHz)	Synthesized beam (arcsec × arcsec)	Δv (km s^{-1})	rms (mJy)
0	86.58–87.05	1.45 × 1.04	0.84	2.0
1	88.50–88.97	1.41 × 1.02	0.83	2.0
2	99.00–99.23	1.28 × 0.92	0.74	1.4
3	101.10–101.57	1.25 × 0.90	0.72	2.3

The data were calibrated and imaged using standard ALMA calibration scripts of the Common Astronomy Software Applications (CASA) package.[1] We imaged with CASA the data cubes, including the continuum, and used them to perform further analysis (see Section 3). The frequency range, synthesized beams, velocity resolution, and rms of the data cubes of the different SPWs are summarized in Table 1. The flux density calibration uncertainty is of 5 per cent, consistent with that of the ALMA band 7 observations of the same source carried out by Jørgensen et al. (2016) and with that estimated from recent analysis of calibrators in bands 3 and 6 (Bonato et al. 2018 and references therein). The analysis of the data was done with the MADCUBA[2] software package.

We have complemented our interferometric ALMA data with publicly available single-dish IRAM 30 m data from the TIMASSS survey consisting of a single pointing towards IRAS16293 (see details in Caux et al. 2011).

3 ANALYSIS

3.1 Continuum

We show in Fig. 1 the 3 mm continuum map towards the two hot corinos: sources A and B. Fig. 2 shows the ALMA spectra towards the continuum peaks of the two sources. In Appendix B we explain in detail how we fitted the continuum emission of both hot corinos in all spectral windows by varying the values of the dust emissivity spectral index β and the dust optical depth τ_{d0}. The best solutions for the continuum fitting are $\beta = 0.9 \pm 0.4$ and $\tau_{d0} = 0.09^{+0.01}_{-0.01}$ for source A and $\beta = 0.0 \pm 0.5$ and $\tau_{d0} = 2.1^{+0.6}_{-0.4}$ for source B. The different values of β might be due to several factors, such as dust chemical composition, size distribution, porosity, and geometry or optical depth effects (see e.g. Ricci et al. 2012; Testi et al. 2014).

[1] https://casa.nrao.edu

[2] Madrid Data Cube Analysis on ImageJ is a software developed at the Center of Astrobiology (Madrid, INTA-CSIC) to visualize and analyse astronomical single spectra and data cubes (Martín et al., in prep.; Rivilla et al. 2016). MADCUBA is available at http://cab.inta-csic.es/madcuba/MADCUBA_IMAGEJ/ImageJMadcuba.html

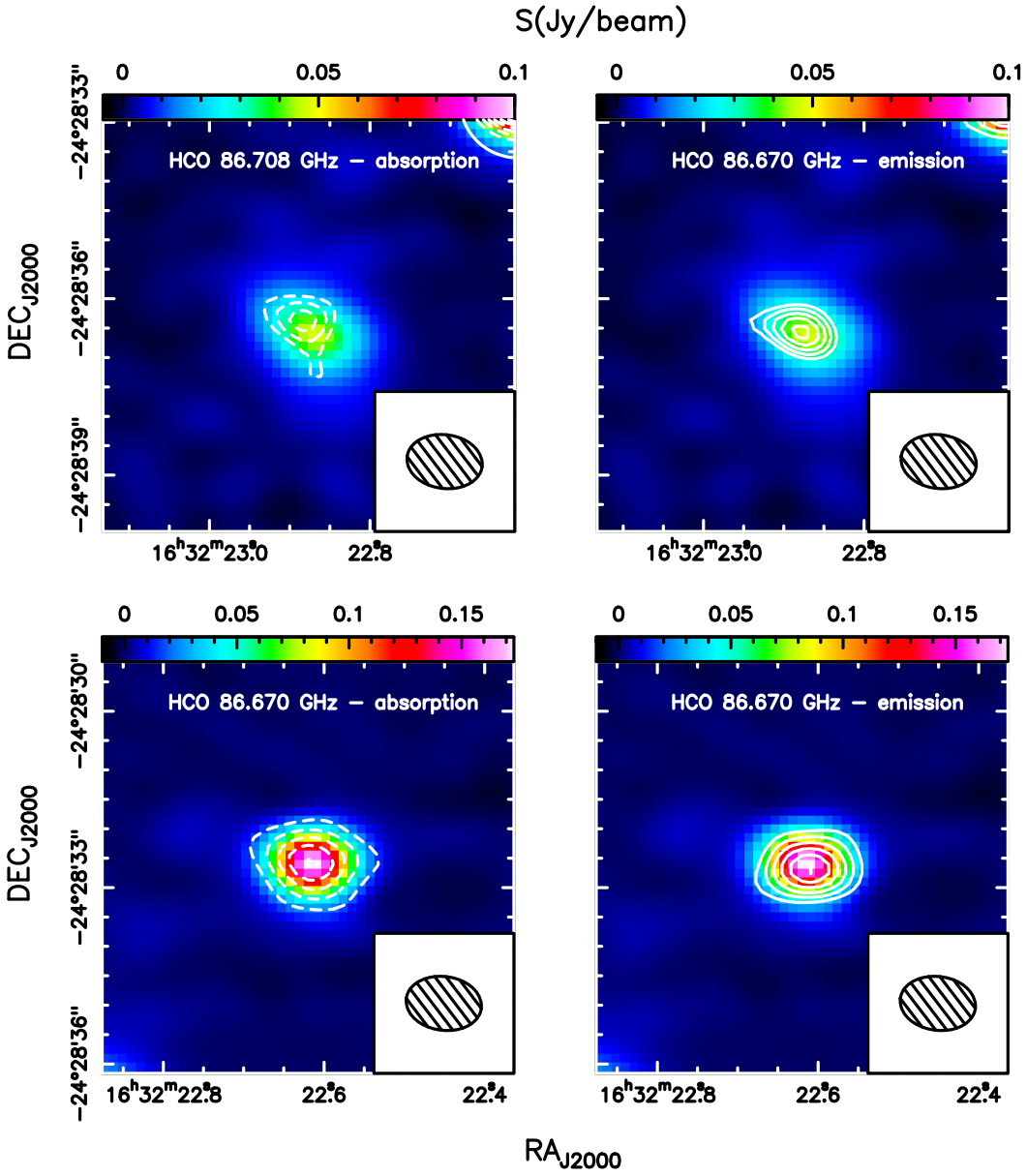

Figure 1. *Upper*: Integrated maps of HCO absorption at 86.708 GHz (velocity range between 3.5 and 4.5 km s^{-1}; left-hand panel) and HCO emission at 86.670 GHz (velocity range between −2 and 4 km s^{-1}; right-hand panel) towards IRAS16293 A. The absorption/emission contours start at − 4/20 mJy beam^{-1} km s^{-1}, with steps of − 1.5/5 mJy beam^{-1} km s^{-1}. The colour scale is the 3 mm continuum emission in Jy beam^{-1}. The beam is indicated in the lower right-hand corner of each panel. *Lower:* Integrated maps of HCO absorption at 86.670 GHz (velocity range between 3.7 and 4.5 km s^{-1}; left-hand panel) and HCO emission at 86.670 GHz (velocity range between 1.2 and 3.6 km s^{-1}; right-hand panel) towards IRAS16293 B. The absorption/emission contours start at − 6/15 mJy beam^{-1} km s^{-1}, with steps of − 5/5 mJy beam^{-1} km s^{-1}.

The resulting continuum levels are shown with red lines in Fig. 2. To create the continuum image we used this continuum level as a reference for selecting the line-free channels, which were used to substract the continuum in the *UV*-plane. The obtained continuum map at ∼94 GHz (Fig. 1) has a synthesized beam of 1.09 × 0.78 arcsec. We obtained the deconvolved size of the continuum sources of A and B at 94 GHz by performing a two-dimensional Gaussian fitting: (1.1 ± 0.1) × (0.7 ± 0.1) arcsec (PA = 45 ± 9) and (0.46 ± 0.03) × (0.42 ± 0.04) arcsec (PA = 148 ± 42), respectively. These sizes are smaller than the synthesized beam of the continuum map, which means that the emission is not resolved. We used these sizes and the synthesized beams of each data cube (Table 1) to calculate the filling factor $f_c(\nu)$ for the continuum fit (see Appendix B).

We used the derived optical depths τ_{d0} to calculate the molecular hydrogen column density of both hot corinos, using the expression $N_{H_2} = \tau_{d0}/(\mu m_H \kappa_0)$, where μ is the mean molecular mass per hydrogen atom (2.8), m_H is the hydrogen mass, and κ_ν is the absorption coefficient per unit density at frequency ν_0. In the calculation we assumed a gas-to-dust mass ratio of 100, and we calculated κ_0 for each source extrapolating from the value at 1 mm of 0.009 cm^2 g^{-1} (thin ices in an H_2 density of 10^6 cm^{-3}; see Ossenkopf & Henning 1994) and using the derived values of β, which gives 0.0044 and 0.009 cm^2 g^{-1} for source A and B, respectively. We obtained $N(H_2)$

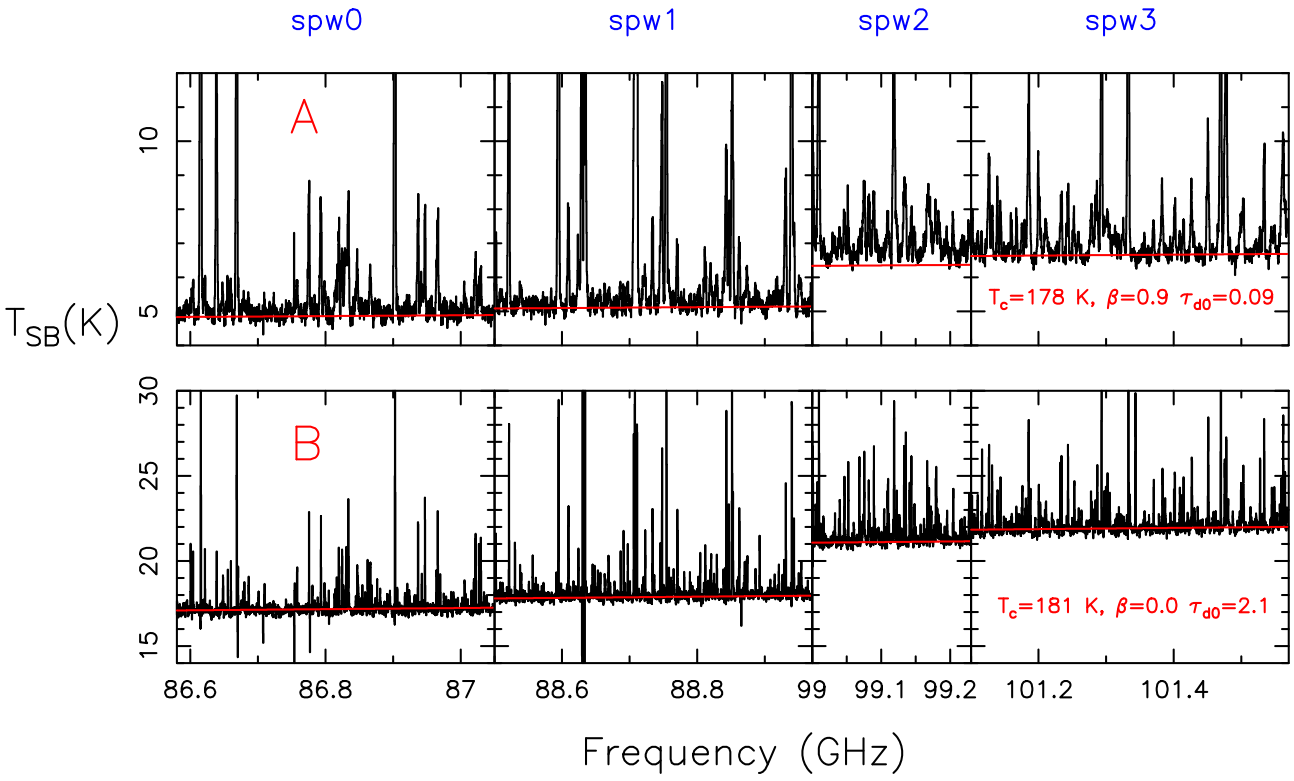

Figure 2. Spectra towards the continuum peak of IRAS16293 source A (upper) and IRAS16293 source B (lower) of the full bandwidth covered by the four different spectral windows. The red lines correspond to the fit of the continuum obtained using a modified blackbody function (see text). The parameters used in the fit are indicated in the right-hand panels.

$= 4.4 \times 10^{24}$ cm^{-2} and $N(H_2) = 5.0 \times 10^{25}$ cm^{-2} for A and B, respectively. These hydrogen column densities are in good agreement with previous estimates: 3.5×10^{24} cm^{-2} for source A (Bottinelli et al. 2004) and ($>$1.2–2.8) $\times 10^{25}$ cm^{-2} (Bottinelli et al. 2004; Jørgensen et al. 2016; Martín-Doménech et al. 2017) for source B.

3.2 Molecular lines

3.2.1 Identification

The identification of the lines was performed using the SLIM (Spectral Line Identification and Modeling) tool of MADCUBA, which uses information from publicly available spectral catalogues. For the analysis of this work we used molecular entries from JPL[3] (Pickett et al. 1998) and CDMS[4] (Müller et al. 2001, 2005; Endres et al. 2016). We searched for the 3 mm quadruplet of HCO, and also for H_2CO, CH_3OH, and CH_2OHCHO lines. In Table 2 we include the transitions of each molecule that are clearly unblended towards source B. In Appendix A we present the line parameters (areas, intensities, v_{LSR}, and full width at half-maximum, FWHW) of the different molecular transitions studied in this work obtained from individual Gaussian fits.

HCO was detected, in emission and redshifted absorption, towards the positions of the two hot corinos. Fig. 1 shows the spatial distribution of HCO, overplotted on the continuum image. The maps show that HCO (the two components, emission and absorption) is not extended but compact in the two protostellar objects, and coincident with the continuum. The deconvolved sizes of the HCO emission and absorption derived by a two-dimensional Gaussian fitting are smaller than the synthesized beam of the data cubes. The same occurs also for H_2CO, CH_3OH, and CH_2OHCHO. Therefore, their spatial distributions are not resolved. For simplicity, we will assume hereafter that the molecular emission/absorption share the same size of the continuum, obtained as $(\theta_{maj} \times \theta_{min})^{0.5}$. This gives 0.88 arcsec for source A and 0.44 arcsec for source B. We note that these sizes are very similar to those used in other works, e.g. 0.9 arcsec for source A (Oya et al. 2016) and 0.5 arcsec for source B (Jørgensen et al. 2016; Ligterink et al. 2017; Martín-Doménech et al. 2017).

Fig. 3 shows the spectra of the HCO quadruplet towards the hot corinos. The brighter HCO line at 86.670 GHz presents a clear inverse P-Cygni profile towards source B, with emission at 2.5 km s^{-1} and absorption at 4.3 km s^{-1}. The absorption is also evident in the other three HCO lines of the quadruplet (upper panels of Fig. 3). A similar P-Cygni profile was also observed in other molecular species, methyl formate (CH_3OCHO), by Pineda et al. (2012). In the case of source A, the HCO line at 86.670 GHz was also detected (see lower left-hand panel in Fig. 3), although it is partially blended with a transition of CH_2DOH, due to the larger linewidths of this source. The absorption component is not clearly seen in this HCO transition, due to the contamination by CH_2DOH. However, the absorption is clear in the HCO transition at 86.70836 GHz (Fig. 3).

In Figs 4 and 5 we show the transitions of the other molecules studied in this work (H_2CO, CH_3OH, and CH_2OHCHO; see Table 2) towards source B and A, respectively. The v_{LSR} and FWHM

[3]https://spec.jpl.nasa.gov
[4]https://www.astro.uni-koeln.de/cdms

Table 2. Molecular transitions of the different species that are clearly unblended towards IRAS16293 source B.

Molecule	Frequency (GHz)	Transition	log A_{ul} (s^{-1})	E_{up} (K)
HCO	86.67076	$1_{0,1} - 0_{0,0}$, J=3/2–1/2, F = 2–1	− 5.3289	4
HCO	86.70836	$1_{0,1} - 0_{0,0}$, J=3/2–1/2, F = 1–0	− 5.3377	4
HCO	86.77746	$1_{0,1} - 0_{0,0}$, J=1/2–1/2, F = 1–1	− 5.3366	4
HCO	86.80578	$1_{0,1} - 0_{0,0}$, J=1/2–1/2, F = 0–1	− 5.3268	4
H_2CO	101.33299	$6_{1,5} - 6_{1,6}$	− 5.8038	88
CH_3OH	86.61560	$7_{2,6} - 6_{3,3}$ − −	− 6.1646	103
CH_3OH	86.90295	$7_{2,5} - 6_{3,4}$ + +	− 6.1596	103
CH_3OH	88.59479	$15_{3,13} - 14_{4,10}$ + +	− 5.9593	328
CH_3OH	88.94009	$15_{3,12} - 14_{4,11}$ − −	− 5.9539	328
CH_2OHCHO	86.60057	$17_{5,2} - 17_{4,13}$	− 4.4770	101
CH_2OHCHO^a	86.86239	$7_{4,3} - 7_{3,4}$	− 4.9138	25
CH_2OHCHO	86.87650	$20_{4,16} - 20_{3,17}$	− 4.8626	427
CH_2OHCHO^a	88.53041	$8_{4,5} - 8_{3,6}$	− 4.8217	30
CH_2OHCHO	88.69126	$12_{3,10} - 12_{2,11}$	− 4.7155	49
CH_2OHCHO	88.89245	$9_{4,6} - 9_{3,7}$	− 4.7558	35
CH_2OHCHO	99.06847	$14_{4,11} - 14_{3,12}$	− 4.5044	67
CH_2OHCHO	101.11631	$21_{4,17} - 21_{3,18}$	− 4.3682	143
CH_2OHCHO^a	101.21981	$18_{3,15} - 18_{2,16}$	− 4.5990	497
CH_2OHCHO	101.23217	$15_{2,13} - 15_{1,14}$	− 4.5990	71
CH_2OHCHO^a	101.51469	$14_{3,12} - 14_{2,13}$	− 5.2467	535
CH_2OHCHO	101.52785	$14_{5,9} - 14_{4,10}$	− 4.73347	74

[a]Transitions used to perform AUTOFIT in source B.

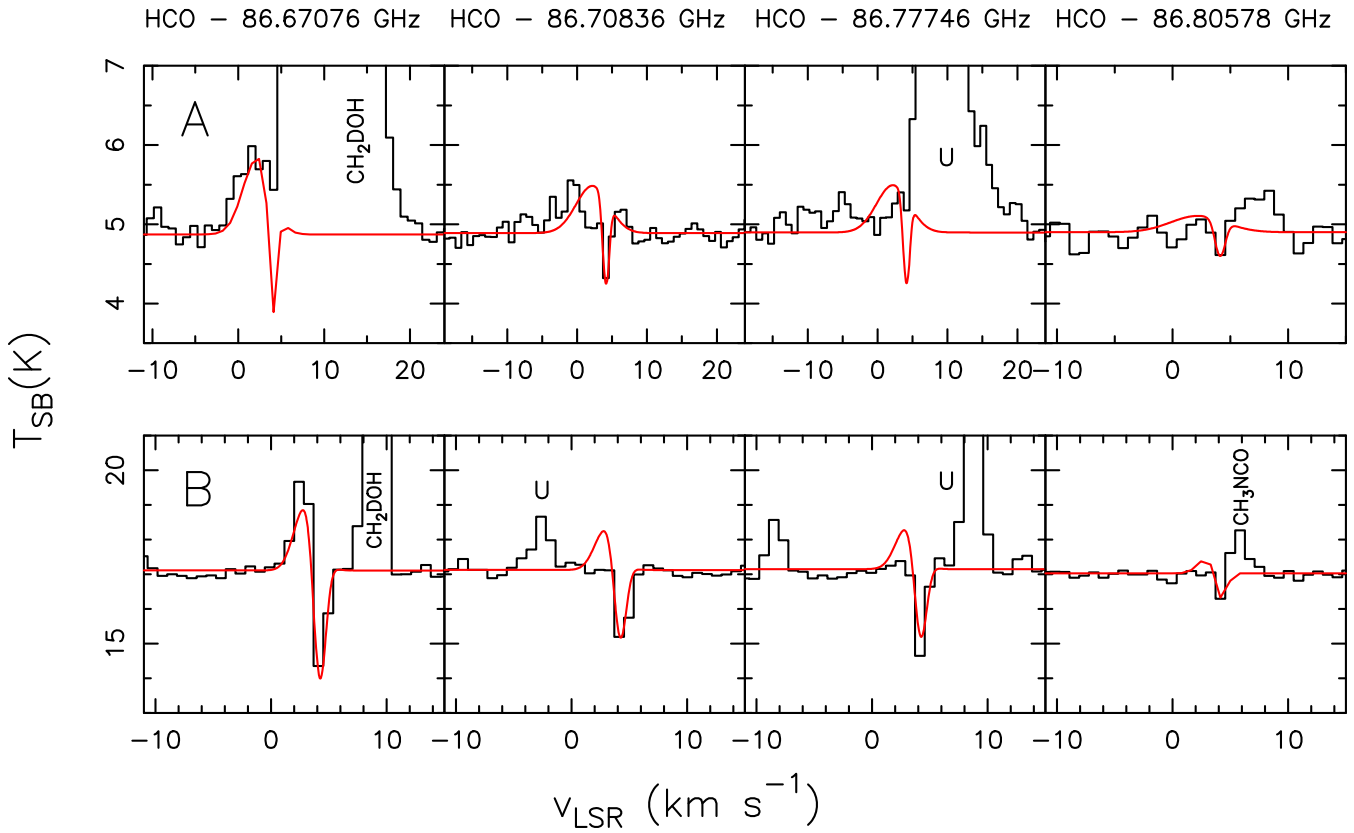

Figure 3. HCO spectra towards the continuum peak of IRAS16293 A (upper) and B (lower). The local thermodynamic equilibrium (LTE) best fits, including the continuum emission, are shown in red curves. Other molecular species in the spectra are also labelled with the their name or with a 'U' if they remain unidentified.

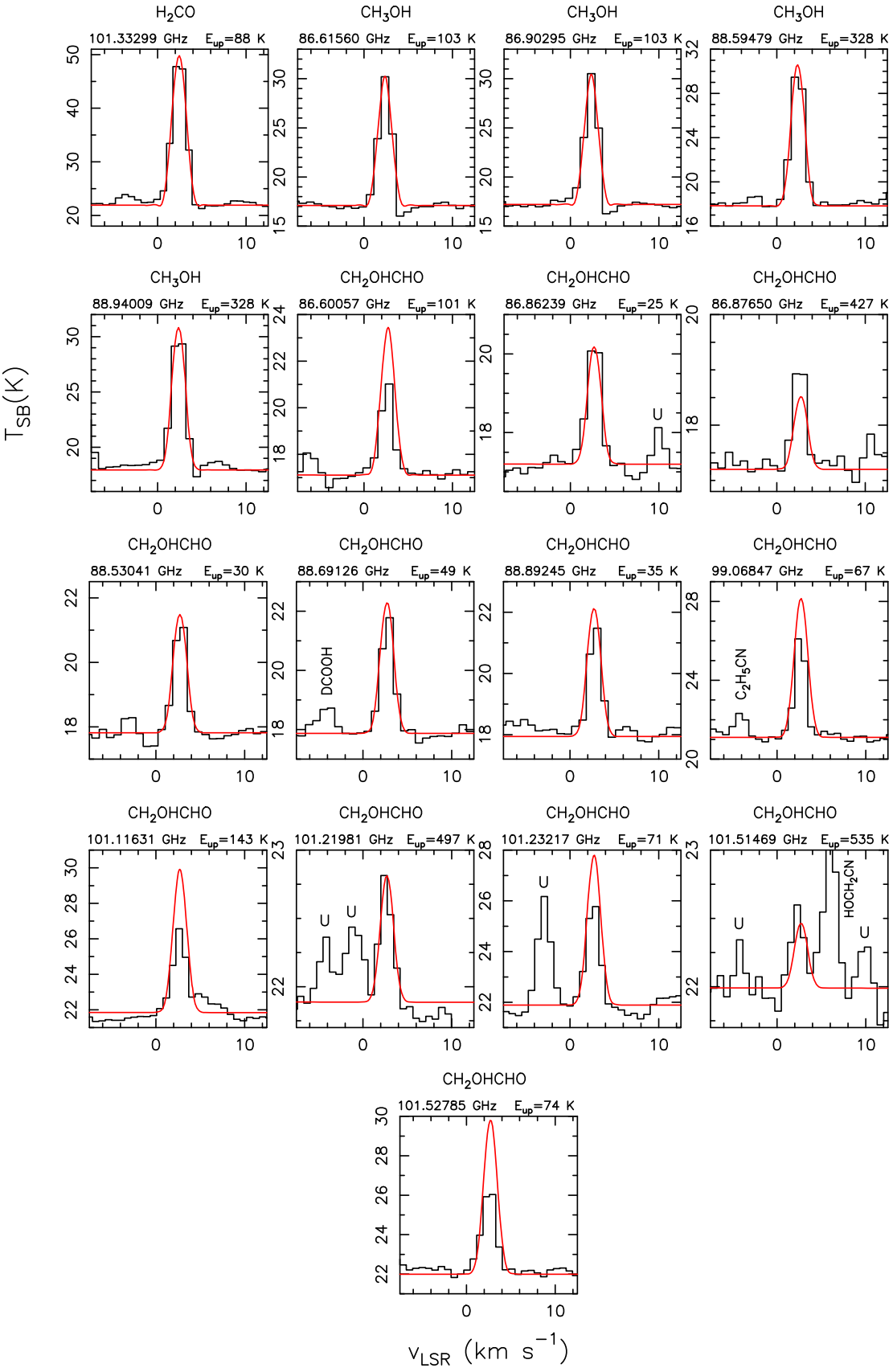

Figure 4. Unblended molecular transitions detected with ALMA of H_2CO, CH_3OH, and CH_2OHCHO towards IRAS16293 source B. The MADCUBA-AUTOFIT LTE best fits, including the continuum, are shown in red. The frequency and E_{up} of each transition are indicated above each panel. Other molecular species in the spectra are also labelled with the their name or with a 'U' if they remain unidentified.

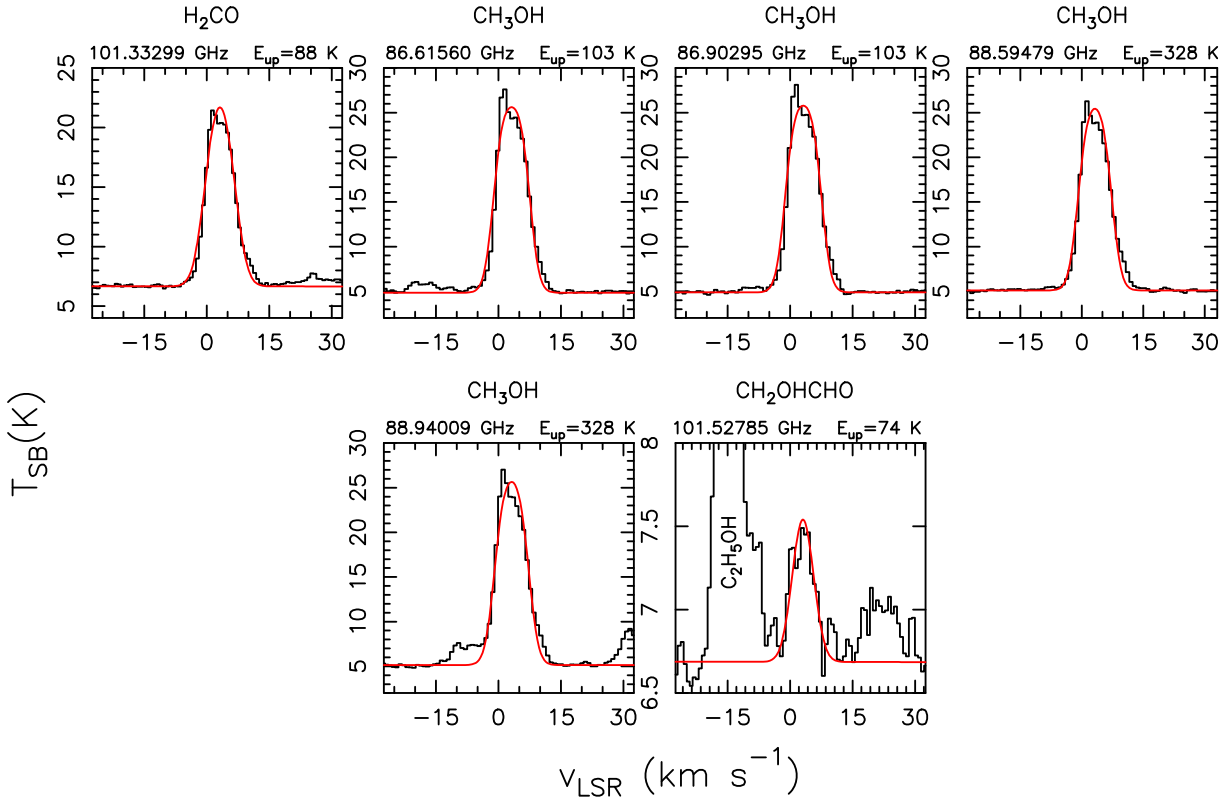

Figure 5. Unblended molecular transitions detected with ALMA of H_2CO, CH_3OH, and CH_2OHCHO towards IRAS16293 source A. The MADCUBA-AUTOFIT LTE best fits, including the continuum, are shown in red. The frequency and E_{up} of each transition are indicated above each panel. Other molecular species in the spectra are also labelled with the their name or with a 'U' if they remain unidentified.

Table 3. Physical parameters obtained with the LTE analysis for the hot corinos IRAS16293 A and B using the ALMA data and for the cold envelope using IRAM 30m data. The parameters derived by using MADCUBA-AUTOFIT include their associated uncertainties, while the parameters that were fixed in the fitting process are shown without uncertainty. For the line opacities, we give the range of values found for the different molecular transitions of each species used in the analysis.

Molecule	T_{ex} (K)	v_{LSR} (km s^{-1})	FWHM (km s^{-1})	N ($\times 10^{16}$ cm^{-2})		Molecular abundance ($\times 10^{-8}$)		τ	$\overline{\chi^2}_{AUTOFIT}$
				this work	other works	this work	other works		
Source A (hot corino)									
HCO (emission)	50	2.2	5.5	0.25	–	0.06	–	0.013–0.064	–
	180	2.2	5.5	1.6	–	0.36	–	0.003–0.017	–
HCO (absorption)	10	4.3	1	0.02 ± 0.01[a]	–	–	–	0.2–0.97	–
H_2CO	100	3.2 ± 0.1	7.1 ± 0.2	15.2 ± 0.4	–	3.4 ± 0.1	10[b]	0.5	0.009
CH_3OH	178 ± 5	3.1 ± 0.1	7.6 ± 0.2	550 ± 12	440 [c]	125 ± 3	77[c]	0.41–0.47	0.02
CH_2OHCHO	110	3.1	7	1.1 ± 0.2	4[d]	0.26 ± 0.03	0.75[d]	0. 02	0.06
	140	3.1	7	1.5 ± 0.2	4[d]	0.34 ± 0.04	0.75[d]	0.016	0.06
Source B (hot corino)									
HCO (emission)	50	2.5	1.8	0.5 ± 0.2	–	0.010 ± 0.003	–	0.08–0.4	0.09
	180	2.5	1.8	3.0 ± 0.7	–	0.06 ± 0.01	–	0.017–0.083	0.09
HCO (absorption)	10	4.3 ± 0.1	1	0.0046 ± 0.0006	–	–	–	0.05–0.26	0.05
H_2CO	100[e]	2.4 ± 0.1	1.3 ± 0.1	23 ± 3	200[f]	0.46 ± 0.06	8.6[f]–10[b]	4	0.006
CH_3OH	181 ± 9	2.4 ± 0.1	1.5 ± 0.1	282 ± 10	850[b] – 2000[g]	5.6 ± 0.2	37[c] – 88[g]	1.0–1.1	0.009
CH_2OHCHO	157 ± 14	2.7 ± 0.1	1.8 ± 0.2	13 ± 3	3–6.8[d, g]	0.27 ± 0.05	0.16–0.35[d, g]	0.02–0.25	0.03
Cold extended envelope									
HCO	10[h]	4.0 ± 0.3	2.2 ± 0.5	(2.6 ± 0.6) × 10^{-4} [i]	[j]	(0.13 ± 0.03) × 10^{-2} [i]	–	0.001–0.006	0.002

[a]The AUTOFIT algorithm did not converge. We selected a good solution by visual inspection, and adopted a conservative uncertainty of 50 per cent. [b]Ceccarelli et al. (2000). [c]Kuan et al. (2004). [d]Jørgensen et al. (2012). [e]We have assumed a source size of 0.65 arcsec for the the fit assuming T_{ex} = 100 K (see text). [f]Persson et al. (2018). [g]Jørgensen et al. (2016). [h]Temperature of the surrounding core of IRAS16293 of 10 K, from van Dishoeck et al. (1995) and Quénard et al. 2018a. [i]Column density averaged in the IRAM 30 m beam. [j]Using the hydrogen column density of the cold envelope reported by van Dishoeck et al. (1995), $N(H_2) = 2 \times 10^{23}$ cm^{-2}.

of these species, shown in Table 3, are in good agreement with those of HCO in both sources. For source A, only the CH_2OHCHO transition at 101.53 GHz (lower panel in Fig. 5) is clearly unblended, while the others are contaminated by other species due to the larger linewidths.

We also did a careful search of the molecular lines that are close to those analysed in this paper in Figs 3, 4, and 5. To identify them, we searched for molecules using JPL and CDMS catalogues in a range of ±1 MHz (which translates to ±3.5 km s^{-1}) around the frequency of the lines. We successfully identified CH_2DOH, CH_3NCO (see Fig. 3), DCOOH, C_2H_5CN and $HOCH_2CN$ (Fig. 4), and C_2H_5OH (Fig. 4). Some lines in the spectra cannot be explained by any of the molecules from the catalogues, and then they remain unidentified (labelled with a 'U'). These lines might be due to species whose spectroscopy is still not available.

3.2.2 *Comparison with single-dish data*

We compared the ALMA spectra with the single-dish spectra observed with the IRAM 30 m telescope, publicly available from the TIMASSS project (Caux et al. 2011). This allows us to determine whether the ALMA observations have missed flux due to filtering and also whether the single-dish telescope was sensitive to gas located in the hot corinos or alternatively in a more extended and colder gas component surrounding the binary system.

In Fig. 6, we show the spectra of HCO, H_2CO, CH_3OH, and CH_2OHCHO obtained with the IRAM 30 m together with those of ALMA integrated in an area matching the IRAM 30 m beam ($\sim$28 arcsec). As seen in this figure, the 3 mm quadruplet of HCO is also clearly detected in emission in the single-dish data (black histogram in upper panels). On the other hand, HCO is not detected in the spatially averaged ALMA spectra (blue histogram in 6; note that the line detected in the left upper panel is CH_2DOH). The emission/absorption detected by ALMA towards the hot corinos discussed previously is clearly diluted in the spatially averaged spectra. This indicates that the HCO emission detected by the IRAM 30 m telescope does not arise from the hot corinos but from a more extended component, probably associated with the circumbinary envelope (e.g. van Dishoeck et al. 1995 and Quénard et al. 2018a), which has been filtered out by ALMA. We note that these ALMA observations had a maximum recoverable scale of $\sim$12 arcsec.

Unlike HCO, the lines of H_2CO and CH_3OH detected with the IRAM 30 m telescope match very well the spatially averaged ALMA spectra, which indicates that the emission detected by the single dish is arising from the compact hot corinos. As seen in Fig. 6, CH_2OHCHO, which has been clearly detected by ALMA (see Figs 4 and 5), is not detected when the emission is averaged over a 28 arcsec area or when observed with the IRAM 30 m due to beam dilution.

Altogether, we can conclude from this comparison that the extended HCO emission observed with the IRAM 30 m comes from the bulk of the circumbinary envelope, and has been filtered out by ALMA, and that the molecular emission (HCO, H_2CO, and CH_3OH) detected with ALMA arises from the hot corinos. The HCO absorption profiles are due to foreground infalling gas of the common circumbinary envelope that is much colder than the hot corinos in the background. This points out the need of using interferometric observations to study the HCO emission associated with the hot corinos/cores.

3.2.3 *Derivation of physical parameters*

To estimate the physical parameters of the different species, we assumed local thermodynamic equilibrium conditions, which is a reasonably good approximation for hot corinos, where the volume densities are very high ($\geq10^8$ cm^{-3}; Jørgensen et al. 2016; Coutens et al. 2018; Quénard et al. 2018a). These densities are several orders of magnitude higher than the critical densities of the H_2CO and CH_3OH transitions considered in this work, which are $\sim10^4$ cm^{-3}, calculated from the collisional coefficients derived by Wiesenfeld & Faure (2013) and Rabli & Flower (2010), respectively. For HCO and CH_2OHCHO, the LTE approach is the only possibility since there are no collisional coefficients available.

To fit the absorption profiles produced by the foreground molecular infalling layer, we used the expression:

$$T_a(\nu) = f_c(\nu)T_c(\nu)e^{-\tau_a(\nu)} + f_a(\nu)T_{ex}^a(1 - e^{-\tau_a(\nu)}),$$

where T_{ex} is the excitation temperature of the absorbing molecular layer, $\tau_e(\nu)$ is the line optical depth of the absorption, $f_c(\nu)$ and $f_a(\nu)$ are the beam filling factors of the continuum and the absorption regions, respectively, and $T_c(\nu)$ is the emission of the background continuum source described in Appendix B. This fit reproduces the absorption lines and also the continuum emission.

To fit the line intensities of the molecular emission from the hot corinos, $T_e(\nu)$, we have used the expression:

$$T_e(\nu) = f_e(\nu)T_{ex}^e(1 - e^{-\tau_e(\nu)}),$$

where T_{ex} is the excitation temperature of the emission, $\tau_e(\nu)$ is the line optical depth of the emission, and $f_e(\nu)$ is the beam filling factor of the emission region. Since the molecular emission and absorption and the continuum emission are not resolved towards both hot corinos, as discussed in Section 3.2.1, we considered the same beam dilution factor for all components, i.e. $f_c(\nu) = f_e(\nu) = f_a(\nu)$, calculated using the continuum sizes presented previously: 0.88 arcsec for source A and 0.44 arcsec for source B.

The MADCUBA-AUTOFIT tool compares the observed spectra with the LTE synthetic spectra of the different species calculated following the previous expressions, taking into account all transitions, and it provides the best non-linear least-squared fit using the Levenberg–Marquardt algorithm. The free parameters of each component (emission and absorption) are as follows: total column density (N), excitation temperature (T_{ex}), velocity (v), and FWHM. MADCUBA-AUTOFIT calculates consistently from these parameters the line opacity for each transition between levels i and j, τ_{ij}, using the expression

$$\tau_{ij} = \frac{h}{\mathrm{FWHM}} N_i B_{ij} (e^{h\nu_{ij}/kT_{ex}} - 1), \quad (1)$$

where B_{ij} is the Einstein B-coefficient, h is the Planck constant, k is the Boltzmann constant and N_i is the column density in the upper level i, which is calculated with the expression:

$$N_i = \frac{N}{Q(T_{ex})} g_i e^{-E_i/kT_{ex}}, \quad (2)$$

where Q is the partition function and g_i and E_i are the degeneracy and the energy of the upper level i, respectively. The derived value of the opacity for each transition is given as output of the fit.

Letting free the four parameters (N, T_{ex}, v, FWHM), MADCUBA-AUTOFIT provides the best combination of parameters with the associated errors. When the algorithm did not converge, we fixed manually the velocities and/or the FWHM to the values that best reproduced the observed spectra and reran AUTOFIT. In some cases, the value of T_{ex} was also fixed (see below). When convergence was

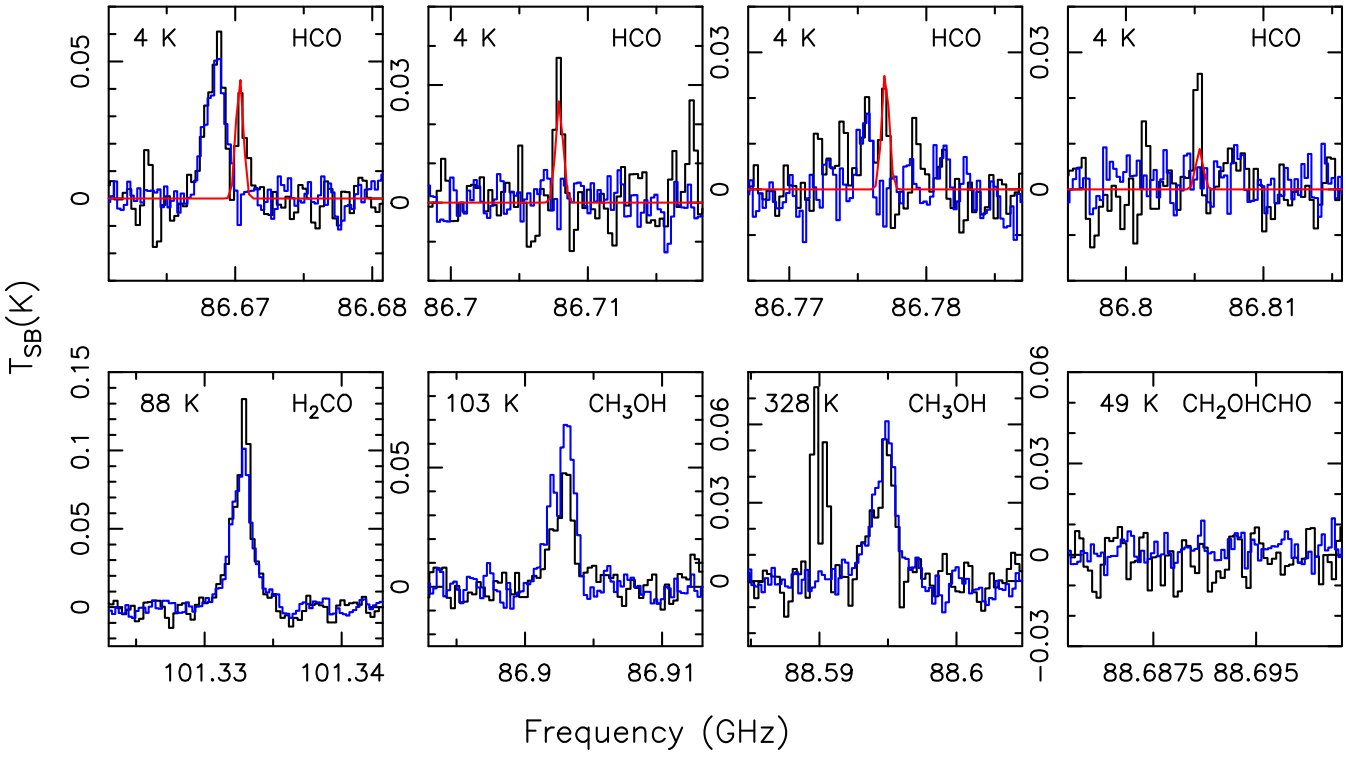

Figure 6. Comparison between IRAM 30 m spectra (black histogram) and the ALMA spectra (blue histogram) integrated in a region coincident with the 30 m beam. Different panels show different transitions. The molecule and the E_{up} are indicated in the right and left upper corners of each panel, respectively. The red curve in the upper panels show the LTE best fit for the HCO detected by the IRAM 30 m telescope.

not possible, we selected by eye the solution that best fit the spectra. The physical parameters derived are shown in Table 3. The errors of the parameters left free are derived from the diagonal elements of the covariance matrix, the inverse of the Hessian Matrix, and the final χ^2 of the fit. The ratio between the errors and the values of each parameter gives a qualitative idea of the goodness of the fit. Furthermore, in Table 3 we include the normalized $\overline{\chi^2}$ value of the fit, which was calculated dividing the χ^2 by the signal to noise of the analysed transitions.

We were not able to derive the excitation temperature of HCO because the four detected lines of HCO share the same E_{up}, 4 K. Since the ALMA maps (Fig. 1) show that the HCO emission arises from the hot corinos (see also Section 3.2.2), we then assumed a range of temperatures typical of hot corinos, 50–180 K, which encompasses the values found for many other molecular tracers in the literature (e.g. Kuan et al. 2004; Martín-Doménech et al. 2017) and the ones we obtain from CH_3OH and CH_2OHCHO in this data set (see below). The derived value of the HCO column density can vary up to a factor of 6 in the adopted temperature range. We will find in Section 4 that the predictions of our chemical model favour a temperature for HCO of ∼70 K, within the range considered here. For the HCO component in absorption, which is expected to arise from foreground and colder gas, we assumed the temperature of 10 K of the surrounding circumbinary envelope of IRAS16293 (van Dishoeck et al. 1995 and Quénard et al. 2018a). The LTE fits of HCO in sources A and B, including both emission and absorption components, are shown with red curves in Fig. 3. We note that while the brightest HCO transition at 86.670 GHz is detected in emission towards both hot corinos at detection levels $>5\sigma$, the other weaker transitions of the quadruplet are not clearly detected in emission. This might be due to a combination of several effects: weak line emission, noise of the spectra, modest spectral resolution, and the presence of the absorption profiles. To prove this, we simulated the HCO spectra (emission + absorption) using the physical parameters resulting from the fit (Table 3), mimicking the spectral resolution and the rms of the observed spectra. We performed many different simulations in which the noise was created randomly. We also applied different spectral resamplings; i.e., we shifted slightly the position of the channels by values lower than the channel width. Our results show that while the brightest HCO transition is always detected above 5σ, the other transitions can be spectrally diluted and fall below 2–3σ levels, which would explain why they are not clearly detected in our observations. A similar spectral dilution effect of an inverse P-Cygni profile was observed in Herschel observations of the L1544 prestellar core with different spectral resolutions (Caselli et al. 2012).

The LTE fits of the other molecules are shown in Figs 4 (source B) and 5 (source A). For CH_3OH and CH_2OHCHO, for which multiple transitions with different E_{up} were observed (Table 2), we left T_{ex}^{e} as a free parameter, and were able to derive its value. For CH_3OH, we obtained $T_{ex}^{e} = 178 \pm 5$ K and 181 ± 9 K for source A and B, respectively, which confirms that the methanol emission arises from the hot corinos. For CH_2OHCHO, most of the unblended lines towards source B are low energy levels (Table 2). To avoid a bias towards low energies, we have selected two transitions at low energies and two transitions at high energies (indicated in Table 2) to perform AUTOFIT. We obtained a temperature of 157 ± 14 K for source B, similar to that obtained for CH_3OH, and a column density of $(13 \pm 3) \times 10^{16}$ cm^{-2} (Table 3). For source A, the only clearly unblended transition of CH_2OHCHO is that at 101.527 GHz (E_{up} = 74 K) . The excitation temperatures found in other studies for source A are typically a factor 0.7–0.9 lower than those of source

B (Kuan et al. 2004; Jørgensen et al. 2012, 2016). Therefore, we considered the temperature derived for source B and applied this range of factors, which gives $T_{ex}^{e} \sim 110-140$ K. Fixing these temperatures, we fitted the CH_2OHCHO transition at 101.527 GHz, and we obtained column densities of (1.1–1.5) $\times$ 10^{16} cm^{-2} (Table 3).

The column density derived for CH_3OH in source B is 2.8 $\times$ 10^{18} cm^{-2}. We have searched in the literature other estimates of the CH_3OH column density obtained from interferometric observations. For source B, Kuan et al. (2004) reported a value of 5 $\times$ 10^{17} cm^{-2} averaged in a synthesized beam of 1.2 $\times$ 2.6 arcsec. Considering the source size that we have adopted, 0.44 arcsec, this translates into $\sim$8.5 $\times$ 10^{18} cm^{-2}, which is about a factor of 3 higher than our value. Jørgensen et al. (2016) found a column density one order of magnitude higher than our value. The low value we found could be due to optical depth effects. Jørgensen et al. (2016) did not use CH_3OH but the isotopologue $CH_3^{18}OH$, which is expected to be optically thinner, and then used the standard ISM $^{16}O/^{18}O$ ratio of 560 (Wilson & Rood 1994). However, the $^{16}O/^{18}O$ ratio might be uncertain. It has been found that other fractionation ratios, such as the $^{12}C/^{13}C$ ratio, are usually lower in hot corinos/cores than in the ISM by a factor of $\sim$2 (Jørgensen et al. 2016) or even of 4–5 (Beltrán et al. 2018). However, Persson et al. (2018) found a $^{16}O/^{18}O$ ratio in source B that is not lower than the ISM value but higher, with a value of $\sim$805. Using this value, the CH_3OH column density derived by Jørgensen et al. (2016) would be a factor of 1.4 higher. Therefore, the most likely explanation for the low value we derived is optical depth. MADCUBA−SLIM, as explained before, calculates consistently the line opacity of each transition, and takes it into account in the calculation of the column density. Namely, if the source size and the T_{ex} are reasonably well known, the derived value of N is good whenever the fitted lines are optically thin. If the lines are optically thick, the derived N should be considered as a lower limit, because the LTE line profile flattens and the line intensity becomes independent of N. The opacities derived with MADCUBA-AUTOFIT for the transitions of CH_3OH are 1.0–1.1 for source B (Table 3). Therefore, the lines are not optically thin, and our estimates of the CH_3OH column densities should be considered as strict lower limits. Regarding source A, Kuan et al. (2004) found a value of 4.4 $\times$ 10^{18} cm^{-2} (after correction for the source size), which is very similar to our estimate of 5.5 $\times$ 10^{19} cm^{-2}. However, given the relatively high optical depth derived in our data (0.41–0.47, Table 3), these values should be considered as lower limits.

For H_2CO, we only have one transition, so T_{ex}^{e} cannot be derived. We have used an excitation temperature of 100 K, like that found by van Dishoeck et al. (1995) and Persson et al. (2018). We obtained a column density of (15.2 $\pm$ 0.4) $\times$ 10^{16} cm^{-2} for source A. For source B, the LTE fit assuming T_{ex}^{e} = 100 K saturates at a line intensity of $\sim$35 K, while the observed line temperature is $\sim$50 K (Fig. 4). This may indicate that the H_2CO emission is slightly larger than the 0.44 arcsec size we have assumed. Considering a larger size of 0.65 arcsec (still smaller than our beam), the line is well reproduced with a column density of (23 $\pm$ 3) $\times$ 10^{16} cm^{-2}, which is one order of magnitude lower than that found by Persson et al. (2018) (Table 3). We note that the derived opacity of the line is high, $\sim$4, which indicates that this line is optically thick towards source B, and that therefore we are underestimating its column density.

To derive the molecular abundances of the different species we have used molecular hydrogen column densities calculated previously: $N(H_2)$ = 4.4 $\times$ 10^{24} cm^{-2} and $N(H_2)$ = 5.0 $\times$ 10^{25} cm^{-2} for A and B, respectively, The resulting molecular abundances are shown in Table 3. For source A, the HCO abundance is (0.06–0.36) $\times$ 10^{-8}, for the range of excitation temperature considered. The molecular abundances obtained for the other species (H_2CO, CH_3OH, and CH_2OCHO) are similar to previous estimates (Table 3) within factors 2–3.

For source B, the HCO abundance is (0.01–0.06) $\times$ 10^{-8}, which is a factor of 6 lower than for source A. As discussed before, CH_3OH may be suffering optical depth effects, which could explain why our abundance is a factor of 5 and 16 lower than that estimated by Kuan et al. (2004) and Jørgensen et al. (2016), respectively. The situation is similar for H_2CO, for which we have found an abundance more than one order of magnitude lower than that found by Ceccarelli et al. (2000) and Persson et al. (2018). The abundance of CH_2OHCHO is very similar to that found by Jørgensen et al. (2012, 2016).

We also derived the column density of the extended HCO component detected by the IRAM 30 m telescope by fitting the HCO quadruplet shown in black in Fig. 6. We assumed that the emission fills the telescope beam and used as T_{ex} the kinetic temperature of $\sim$10 K estimated for the surrounding circumbinary envelope of IRAS16293 (van Dishoeck et al. 1995; Quénard et al. 2018a). The fit obtained with MADCUBA-AUTOFIT is shown in Fig. 6. We note that the observed intensities of the lines of the HCO quadruplet are not fully reproduced by the LTE fit. In particular, the lines at 86.70836 GHz and 86.80578 GHz are brighter than the LTE prediction, which may indicate that HCO in the cold circumbinary envelope is not in LTE. However, since collisional coefficients of this species are not available, we performed an LTE analysis. The derived parameters are shown in Table 3. We obtained a column density of (3–5) $\times$ 10^{12} cm^{-2}, which translates into an abundance of (1.5–2.9) $\times$ 10^{-11} by using the column density of the cold circumbinary envelope estimated by van Dishoeck et al. (1995), which is N_{H_2} = 2 $\times$ 10^{23} cm^{-2}. This HCO abundance is significantly lower by 1–2 orders of magnitude than that found in the hot corinos.

4 COMPARISON WITH THE CHEMICAL MODEL

To identify the most likely chemical routes to form HCO and its role in forming more complex species such as CH_3OH and CH_2OHCHO, we used an updated chemical model based on Vasyunin & Herbst (2013b). This schematic zero-dimensional model mimics the evolution of a parcel of gas and dust with time-dependent physical conditions from a diffuse cloud to a hot corino. The model consists of two stages. During the first stage, a free-fall collapse occurs (Brown et al. 1988; Spitzer 1998). Physically, this stage is attributed to the formation of a cold and dense core from a translucent cloud. The collapse occurs over 10^6 yr. During this time, gas density increases from the initial value of 3 $\times$ 10^3 cm^{-3} to the final value of 10^8 cm^{-3}, which matches the typical densities of hot corinos (see e.g. Woods et al. 2013; Awad et al. 2014; Coutens et al. 2018). Visual extinction changes correspondingly from the starting value of A_v = 2, and gas and dust temperatures are assumed to be equal. During the collapse, the dust temperature drops from $\sim$20 K to $\sim$10 K due to less efficient radiative heating of dust grains in a dark, dense cloud in comparison to a translucent cloud exposed to UV radiation (Garrod & Pauly 2011). The second stage is a warm-up phase. It is assumed that during this stage a parcel of gas and dust warms up from 10 K to 200 K during 2 $\times$ 10^5 yr, developing into a hot corino. The gas density during the second stage remains constant. We would like to note that despite the simplicity of such a model, it has been proven to be a powerful tool to explore the chemistry of

hot cores and corinos by a number of studies (see e.g. Brown et al. 1988; Rawlings et al. 1992; Viti & Williams 1999; Viti et al. 2004; Garrod & Herbst 2006; Vasyunin & Herbst 2013a; Rivilla et al. 2016). Thus, we stick to this simplistic physical model, although more advanced treatment is planned for future detailed studies.

The chemical network used in this study is based on an updated version of the one presented in Vasyunin et al. (2017). Several important updates were introduced to accurately treat the chemistry of HCO and CH_2OHCHO. We note that the results of astrochemical models, including the one presented in this work, are intrinsically uncertain by at least an order of magnitude (Vasyunin et al. 2004, 2008; Wakelam et al. 2005; Wakelam, Herbst & Selsis 2006; Wakelam et al. 2010). Thus, for the molecular abundances predicted by the model we have considered an uncertainty range multiplying and dividing by a factor of 3.

4.1 The formation of HCO: surface chemistry, gas-phase chemistry, or both?

Different chemical routes have been proposed to form HCO, both in the surface of dust grains (Tielens & Hagen 1982; Brown et al. 1988; Dartois et al. 1999; Watanabe & Kouchi 2002; Woon 2002; Bacmann & Faure 2016) and in the gas phase (Bacmann & Faure 2016; Hickson et al. 2016). The scheme of the chemical network including all these reactions is presented in Fig. 7. To evaluate the role of surface chemistry in the formation of HCO, we have run the three different models (I, II, and III) presented in Table 4 (see also Fig. 7). We also considered different reactions that can destroy HCO (see Fig. 7), both in the gas phase and on the grain surface. As we will discuss in Section 4.2, HCO is involved in several chemical routes to form CH_2OHCHO. For simplicity, in this section we only considered the route involving HCO and CH_2OH, which is the most efficient according to our model (see Section 4.2).

The role of surface chemistry routes in determining the gas-phase abundance of HCO is different during the cold collapse phase and the warm-up phase. In the cold phase, the abundance of HCO is almost independent of the details of the surface chemistry, and is mainly maintained by the gas-phase reaction [2] (Table 4). Fig. 8 shows that the abundance predicted by the chemical model I, which considers only gas-phase chemistry, is around several $\sim 10^{-11}$ at the expected volume density of the cold envelope, $3 \times 10^4 - 2 \times 10^5$ cm^{-3} (from van Dishoeck et al. 1995 and Quénard et al. 2018a). This value is in good agreement with the abundance derived for the extended cold component (see Table 3), indicating that gas-phase formation routes are sufficient to consistently explain the HCO abundance in the cold envelope. This is also in agreement with Bacmann & Faure (2016), who reached the same conclusion in a survey of low-mass pre-stellar cores.

During the protostellar phase, the contribution of the grain surface is much more important. In particular, model II, which includes the surface hydrogenation of CO (reaction [3] in Table 4), produces a peak of HCO abundance of several 10^{-10}, similar to the ones found in IRAS16293 A and B when a temperature of 50 K was assumed, which is higher than the abundances produced by models I and III by more than an order of magnitude (Fig. 9). The peak of HCO abundance in the model is reached at a warm temperature of ∼60–70 K. At higher temperatures, HCO is progressively destroyed through the gas-phase reaction between HCO and atomic hydrogen (Hebrard et al. 2009). This reaction is very efficient in hotter gas because the abundance of atomic hydrogen is significantly higher than in cold gas. Therefore, the chemical model is suggesting that the emission of HCO detected by ALMA is arising for a warm component of the hot corinos at a temperature ∼60–70 K, rather than from hotter gas (>100 K). Since we were not able to derive the excitation temperature of HCO, in Section 3 we assumed two temperatures, 50 and 180 K, to derive its abundance. Indeed, the HCO abundances derived assuming 50 K, which are a factor ∼6 lower, match better the peak abundances of HCO predicted by the model (at 60–70 K). This is further evidence pointing towards a warm origin of the HCO observed in emission by ALMA.

4.2 HCO as precursor of COMs

HCO has been proposed as the basic precursor of many COMs, and in particular of CH_2OHCHO. Woods et al. (2012, 2013) tested theoretically different mechanisms of CH_2OHCHO synthesis previously proposed in the literature (e.g. Sorrell 2001; Charnley & Rodgers 2005; Halfen et al. 2006; Bennett & Kaiser 2007; Garrod et al. 2008; Beltrán et al. 2009), both in the gas phase and on the surface of grains, and concluded that the most likely pathways are three grain-surface formation routes involving HCO. To explore the possible formation routes of CH_2OHCHO, we considered several routes recently discussed in the literature (Garrod et al. 2008; Woods et al. 2012, 2013; Fedoseev et al. 2015; Chuang et al. 2016). In all these routes, the availability of HCO is a key condition. All routes of formation of HCO considered in the previous section were switched on.

Therefore, to test the viability of these chemical pathways to form CH_2OHCHO, we have compared the molecular abundances estimated in IRAS16293 with the output of the considered models. Since the detailed modelling of CH_2OHCHO chemistry will be presented in a separate paper (Vasyunin et al., in prep.), below we only focus on the chemical pathway that showed the best agreement with observations presented in this study.

The model that better fits the observations is the model where CH_2OHCHO is produced by the surface reaction between HCO and CH_2OH. It produces a peak of HCO of $\sim 0.07 \times 10^{-8}$ at 60–70 K, which is of the order of that derived for sources A and B if we assume $T_{ex} = 50$ K (see left-hand panel of Fig. 10). For CH_3OH, the observed abundances are reasonably well reproduced for temperatures ≥110 K (Fig. 10), which are not far from the excitation temperature derived from observations (see Table 3).

The abundance of H_2CO derived from observations is reached at a temperature of ∼60 K in the model (Fig. 10), similar to the temperature at which the abundance of HCO peaks according to the model. This may indicate that HCO and H_2CO are tracing warm gas of the hot corinos, instead of the hotter gas (T >100 K) traced by CH_3OH and CH_2OHCHO. Alternatively, if H_2CO traces hot gas at ∼100 K, as suggested by the excitation temperature found by van Dishoeck et al. (1995) and Persson et al. (2018), then the model is overproducing H_2CO by ∼2 orders of magnitude compared to observed values.

Finally, CH_2OHCHO in the model reaches an abundance similar to that estimated from the observations for a temperature of ∼140 K, which is consistent with the T_{ex} derived from the observations. This temperature is higher than that at which HCO peaks in the model (∼70 K). This is because CH_2OHCHO, which is formed at low temperatures through the surface reaction $HCO + CH_2OH \rightarrow CH_2OHCHO$, has much higher desorption energy than HCO (6684 K versus 1600 K; Garrod et al. 2008), and then it is desorbed later when the temperature increases.

In summary, we favour the reaction between HCO and CH_2OH as the most likely chemical route for the formation of CH_2OHCHO. However, we do not aim at completely rule out other surface

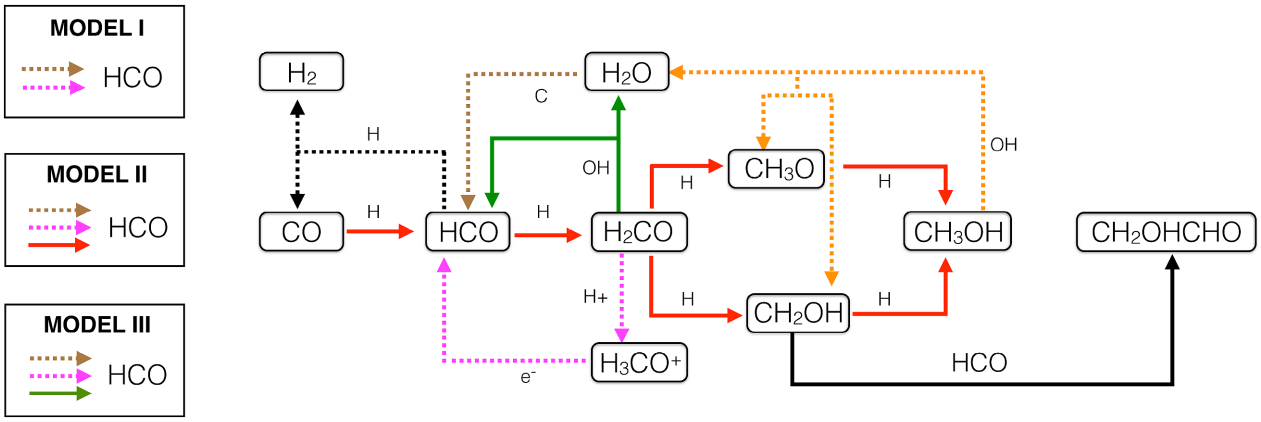

Figure 7. Chemical routes discussed in this work and implemented in our chemical model to study the formation of HCO. The solid and dashed arrows indicate gas-phase and grain-surface reactions, respectively. On the left, we indicate with boxes the three different models (I, II, and III) we considered for the formation of HCO. We indicate with arrows within each box the reactions that were included in each model, following the same colour and stroke code as in the diagram. We have also added the most efficient formation route of CH_2OHCHO according to our model (Section 4.2).

Table 4. Chemical models considered for the formation of HCO.

Model I	
$H_2CO + H^+ \longrightarrow H_3CO^+ ; H_3CO^+ + e^- \longrightarrow HCO + H + H$ (gas)	[1]
$C + H_2O \longrightarrow HCO + H$ (gas)	[2]
Model II	
Model I + CO $\longrightarrow$ HCO $\longrightarrow$ $H_2CO \longrightarrow CH_3OH$ (surface)	[3]
Model III	
Model I + OH + $H_2CO \longrightarrow$ HCO + H_2O (surface)	[4]

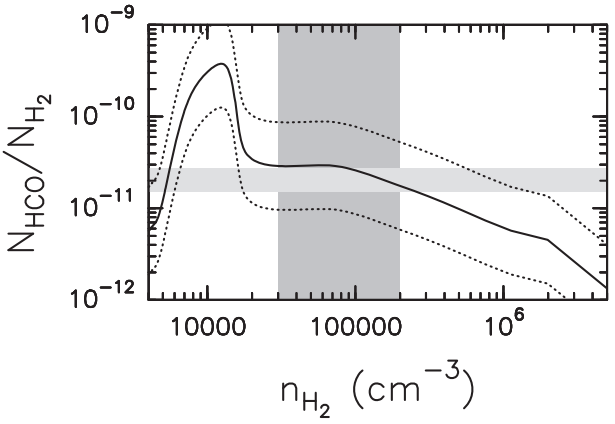

Figure 8. Results of the chemical model I (gas-phase chemistry) during the cold collapse phase. The evolution of the molecular abundance of HCO is represented as a function of the volume density with a solid black curve. The area within the dotted black curves delimits the uncertainty of the chemical model, obtained by multiplying and dividing the outcome of the model by a factor of 3. The vertical dark grey band is the volume density derived by van Dishoeck et al. (1995) and Quénard et al. (2018b) for the cold envelope of IRAS16293: $3 \times 10^4 - 2 \times 10^5$ cm^{-3}. The horizontal light grey band indicates the range of HCO abundances derived from the IRAM 30 m observations (Table 3).

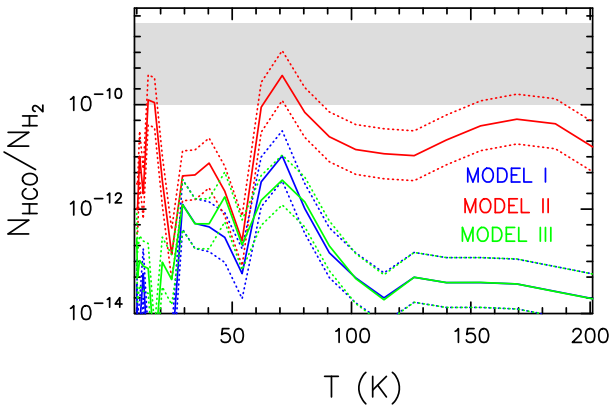

Figure 9. Results of the chemical models (I, II, and III) during the protostellar warm-up phase. The evolution of the molecular abundance of HCO is represented as a function of temperature. The area within the dotted curves delimits the uncertainty of the chemical model, obtained by multiplying and dividing the output of the model by a factor of 3. Model I (blue) includes only gas-phase reactions; model II (red) includes gas-phase reactions and the surface hydrogenation of CO; and model III (green) includes gas-phase reactions and the surface reaction $H_2CO + OH \rightarrow HCO + H_2CO$. The horizontal light-grey band indicates the range of HCO abundances found in the ALMA observations (Table 3).

chemistry routes recently considered in laboratory experiments (Fedoseev et al. 2015; Chuang et al. 2016) and chemical modelling (Woods et al. 2012, 2013; Coutens et al. 2018). A more complete and detailed analysis of all routes of formation of CH_2OHCHO, including also the recently proposed gas-phase route by Skouteris et al. (2018), will be presented in a forthcoming paper (Vasyunin et al., in prep.).

5 SUMMARY AND CONCLUSIONS

The formyl radical HCO has been proposed as the fundamental precursor of many complex organic molecules. We presented the first high spatial resolution maps of HCO using ALMA towards the solar-type protostellar binary IRAS16293–2422. We also detected several lines of the chemically related species formaldehyde (H_2CO), methanol (CH_3OH), and glycolaldehyde (CH_2OHCHO).

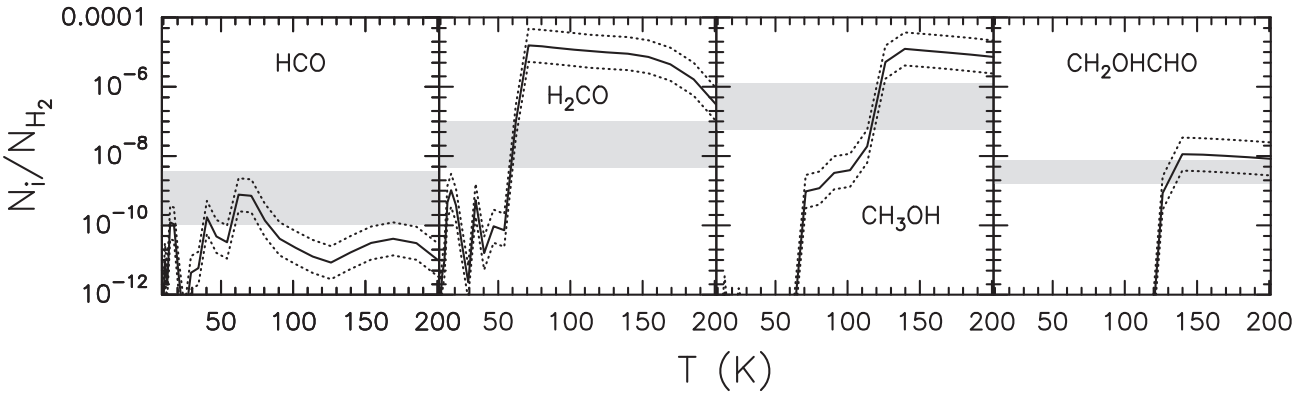

Figure 10. Results of the chemical model that better fits the molecular abundances of the species studied in this work. We show the molecular abundances as a function of the temperature with solid curves. The area within the dotted curves delimits the uncertainty of the chemical model, obtained multiplying and dividing the model result by a factor of 3. The horizontal light-grey bands indicate the range of abundances found in the observations for source A and B (Table 3).

The HCO emission is compact and arises from the hot corinos surrounding the two protostars. The line profiles also exhibit red-shifted absorption produced by foreground infalling material of the circumbinary cold envelope. Previous IRAM 30 m single-dish observations detected more extended HCO emission from the circumbinary envelope. To identify the most likely chemical routes to form HCO, and to determine its role in forming more complex species, we compared the observed molecular abundances with the predictions of our chemical model, which takes both gas-phase and grain-surface chemistry into account. We find that while the HCO in the envelope can be explained considering only pure gas-phase reactions, the HCO detected in the hot corinos needs the hydrogenation of CO on the surface of dust grains to be formed. Subsequent surface hydrogenation of HCO and thermal desorption are also responsible for the observed abundances of H_2CO and CH_3OH. We also find that the main formation route of CH_2OHCHO is the surface reaction between HCO and CH_2OH. The detailed contribution of other chemical routes, including gas-phase reactions, will be carefully studied in a forthcoming theoretical paper.

ACKNOWLEDGEMENTS

We thank the anonymous referee for her/his constructive comments that contributed to improve the manuscript. This project has received funding from the European Union's Horizon 2020 research and innovation programme under the Marie Skłodowska-Curie grant agreement No 664931, and from the Italian Ministero dell'Istruzione, Università e Ricerca through the grant Progetti Premiali 2012 – iALMA (CUP C52I13000140001). The work by A. V. is supported by the Russian Science Foundation via the project 18-12-00351. This paper makes use of the following ALMA data: ADS/JAO.ALMA#2015.1.01193.S ALMA is a partnership of ESO (representing its member states), NSF (USA) and NINS (Japan), together with NRC (Canada), NSC, and ASIAA (Taiwan), and KASI (Republic of Korea), in co-operation with the Republic of Chile. The Joint ALMA Observatory is operated by ESO, AUI/NRAO and NAOJ.

REFERENCES

Agúndez M., Cernicharo J., Guélin M., 2015, A&A, 577, L5
Awad Z., Viti S., Bayet E., Caselli P., 2014, MNRAS, 443, 275
Bacmann A., Faure A., 2016, A&A, 587, A130
Balucani N., Ceccarelli C., Taquet V., 2015, MNRAS, 449, L16
Belloche A., Garrod R. T., Müller H. S. P., Menten K. M., Comito C., Schilke P., 2009, A&A, 499, 215
Belloche A. et al., 2017, A&A, 601, A49
Beltrán M. T., Codella C., Viti S., Neri R., Cesaroni R., 2009, ApJ, 690, L93
Beltrán M. T. et al., 2018, A&A, 615, A141
Bennett C. J., Kaiser R. I., 2007, ApJ, 661, 899
Bergantini A., Góbi S., Abplanalp M. J., Kaiser R. I., 2018, ApJ, 852, 70
Bonato M. et al., 2018, MNRAS, 478, 1512
Bottinelli S. et al., 2004, ApJ, 617, L69
Brown P. D., Charnley S. B., Millar T. J., 1988, MNRAS, 231, 409
Butscher T., Duvernay F., Theule P., Danger G., Carissan Y., Hagebaum-Reignier D., Chiavassa T., 2015, MNRAS, 453, 1587
Caselli P., Ceccarelli C., 2012, A&AR, 20, 56
Caselli P. et al., 2012, ApJ, 759, L37
Caux E. et al., 2011, A&A, 532, A23
Cazaux S., Tielens A. G. G. M., Ceccarelli C., Castets A., Wakelam V., Caux E., Parise B., Teyssier D., 2003, ApJ, 593, L51
Ceccarelli C., Loinard L., Castets A., Tielens A. G. G. M., Caux E., 2000, A&A, 357, L9
Cernicharo J., Marcelino N., Roueff E., Gerin M., Jiménez-Escobar A., Muñoz Caro G. M., 2012, ApJ, 759, L43
Charnley S. B., Rodgers S. D., 2005, in Lis D. C., Blake G. A., Herbst E., eds, Proc. IAU Symp. Vol. 231, Astrochemistry: Recent Successes and Current Challenges. Cambridge Univ. Press, Cambridge, p. 237
Chuang K.-J., Fedoseev G., Ioppolo S., van Dishoeck E. F., Linnartz H., 2016, MNRAS, 455, 1702
Chuang K.-J., Fedoseev G., Qasim D., Ioppolo S., van Dishoeck E. F., Linnartz H., 2017, MNRAS, 467, 2552
Codella C. et al., 2017, A&A, 605, L3
Coutens A. et al., 2016, A&A, 590, L6
Coutens A., Viti S., Rawlings J. M. C., Beltrán M. T., Holdship J., Jiménez-Serra I., Quénard D., Rivilla V. M., 2018, MNRAS, 475, 2016
Dartois E., Demyk K., d'Hendecourt L., Ehrenfreund P., 1999, A&A, 351, 1066
Dzib S. A. et al., 2018, A&A, 614, A20
Endres C. P., Schlemmer S., Schilke P., Stutzki J., Müller H. S. P., 2016, J. Mol. Spectros., 327, 95
Fedoseev G., Cuppen H. M., Ioppolo S., Lamberts T., Linnartz H., 2015, MNRAS, 448, 1288
Fedoseev G., Chuang K.-J., van Dishoeck E. F., Ioppolo S., Linnartz H., 2016, MNRAS, 460, 4297
Frau P., Girart J. M., Beltrán M. T., 2012, A&A, 537, L9
Garrod R. T., Herbst E., 2006, A&A, 457, 927

Garrod R. T., Pauly T., 2011, ApJ, 735, 15
Garrod R. T., Weaver S. L. W., Herbst E., 2008, ApJ, 682, 283
Gerin M., Goicoechea J. R., Pety J., Hily-Blant P., 2009, A&A, 494, 977
Halfen D. T., Apponi A. J., Woolf N., Polt R., Ziurys L. M., 2006, ApJ, 639, 237
Hebrard E. et al., 2009, J. Phys. Chem. A, 113, 11227
Herbst E., van Dishoeck E. F., 2009, ARA&A, 47, 427
Hickson K. M., Loison J.-C., Nunez-Reyes D., Mereau R., 2016, J. Phys. Chem. Lett., 7, 3641
Jiménez-Serra I., Martín-Pintado J., Rodríguez-Franco A., Marcelino N., 2004, ApJ, 603, L49
Jones B. M., Bennett C. J., Kaiser R. I., 2011, ApJ, 734, 78
Jørgensen J. K., Favre C., Bisschop S. E., Bourke T. L., van Dishoeck E. F., Schmalzl M., 2012, ApJ, 757, L4
Jørgensen J. K. et al., 2016, A&A, 595, A117
Kahane C., Ceccarelli C., Faure A., Caux E., 2013, ApJ, 763, L38
Kuan Y.-J. et al., 2004, ApJ, 616, L27
Ligterink N. F. W. et al., 2017, MNRAS, 469, 2219
Liszt H. S., Pety J., Gerin M., Lucas R., 2014, A&A, 564, A64
Looney L. W., Mundy L. G., Welch W. J., 2000, ApJ, 529, 477
Martín-Doménech R., Rivilla V. M., Jiménez-Serra I., Quénard D., Testi L., Martín-Pintado J., 2017, MNRAS, 469, 2230
Millar T. J., Bennett A., Rawlings J. M. C., Brown P. D., Charnley S. B., 1991, A&AS, 87, 585
Müller H. S. P., Thorwirth S., Roth D. A., Winnewisser G., 2001, A&A, 370, L49
Müller H. S. P., Schlöder F., Stutzki J., Winnewisser G., 2005, J. Mol. Struct., 742, 215
Ossenkopf V., Henning T., 1994, A&A, 291, 943
Oya Y., Sakai N., López-Sepulcre A., Watanabe Y., Ceccarelli C., Lefloch B., Favre C., Yamamoto S., 2016, ApJ, 824, 88
Persson M. V. et al., 2018, A&A, 610, A54
Pickett H. M., Poynter R. L., Cohen E. A., Delitsky M. L., Pearson J. C., Müller H. S. P., 1998, J. Quant. Spec. Radiat. Transf., 60, 883
Pineda J. E. et al., 2012, A&A, 544, L7
Quénard D., Jiménez-Serra I., Viti S., Holdship J., Coutens A., 2018a, MNRAS, 474, 2796
Quénard D., Bottinelli S., Caux E., Wakelam V., 2018b, MNRAS, 477, 5312
Rabli D., Flower D. R., 2010, MNRAS, 406, 95
Rawlings J. M. C., Hartquist T. W., Menten K. M., Williams D. A., 1992, MNRAS, 255, 471
Ricci L., Trotta F., Testi L., Natta A., Isella A., Wilner D. J., 2012, A&A, 540, A6
Rivilla V. M., Fontani F., Beltrán M. T., Vasyunin A., Caselli P., Martín-Pintado J., Cesaroni R., 2016, ApJ, 826, 161
Rivilla V. M., Beltrán M. T., Cesaroni R., Fontani F., Codella C., Zhang Q., 2017a, A&A, 598, A59
Rivilla V. M., Beltrán M. T., Martín-Pintado J., Fontani F., Caselli P., Cesaroni R., 2017b, A&A, 599, A26
Sánchez-Monge Á., López-Sepulcre A., Cesaroni R., Walmsley C. M., Codella C., Beltrán M. T., Pestalozzi M., Molinari S., 2013, A&A, 557, A94
Schenewerk M. S., Snyder L. E., Hjalmarson A., 1986, ApJ, 303, L71
Schenewerk M. S., Jewell P. R., Snyder L. E., Hollis J. M., Ziurys L. M., 1988, ApJ, 328, 785
Schilke P., Pineau des Forêts G., Walmsley C. M., Martín-Pintado J., 2001, A&A, 372, 291
Skouteris D., Balucani N., Ceccarelli C., Vazart F., Puzzarini C., Barone V., Codella C., Lefloch B., 2018, ApJ, 854, 135
Snyder L. E., Hollis J. M., Ulich B. L., 1976, ApJ, 208, L91
Snyder L. E., Schenewerk M. S., Hollis J. M., 1985, ApJ, 298, 360
Sorrell W. H., 2001, ApJ, 555, L129
Spezzano S., Caselli P., Bizzocchi L., Giuliano B. M., Lattanzi V., 2017, A&A, 606, A82
Spitzer L., 1998, Physical Processes in the Interstellar Medium, Wiley
Taquet V., Wirström E. S., Charnley S. B., 2016, ApJ, 821, 46
Testi L. et al., 2014, in Beuther H., Klessen R. S., Dullemond C. P., Henning T., eds, Protostars and Planets VI, University of Arizona Press, Tucson. p. 339
Tielens A. G. G. M., Hagen W., 1982, A&A, 114, 245
van Dishoeck E. F., Blake G. A., Jansen D. J., Groesbeck T. D., 1995, ApJ, 447, 760
Vasyunin A. I., Herbst E., 2013a, ApJ, 762, 86
Vasyunin A. I., Herbst E., 2013b, ApJ, 769, 34
Vasyunin A. I., Sobolev A. M., Wiebe D. S., Semenov D. A., 2004, Astron. Lett., 30, 566
Vasyunin A. I., Semenov D., Henning T., Wakelam V., Herbst E., Sobolev A. M., 2008, ApJ, 672, 629
Vasyunin A. I., Caselli P., Dulieu F., Jiménez-Serra I., 2017, ApJ, 842, 33
Viti S., Williams D. A., 1999, MNRAS, 305, 755
Viti S., Collings M. P., Dever J. W., McCoustra M. R. S., Williams D. A., 2004, MNRAS, 354, 1141
Wakelam V., Selsis F., Herbst E., Caselli P., 2005, A&A, 444, 883
Wakelam V., Herbst E., Selsis F., 2006, A&A, 451, 551
Wakelam V., Herbst E., Le Bourlot J., Hersant F., Selsis F., Guilloteau S., 2010, A&A, 517, A21
Watanabe N., Kouchi A., 2002, ApJ, 571, L173
Wiesenfeld L., Faure A., 2013, MNRAS, 432, 2573
Wilson T. L., Rood R., 1994, ARA&A, 32, 191
Woods P. M., Kelly G., Viti S., Slater B., Brown W. A., Puletti F., Burke D. J., Raza Z., 2012, ApJ, 750, 19
Woods P. M., Slater B., Raza Z., Viti S., Brown W. A., Burke D. J., 2013, ApJ, 777, 90
Woon D. E., 2002, ApJ, 569, 541

APPENDIX A: GAUSSIAN FITS OF THE MOLECULAR TRANSITIONS

We present in Tables A1 and A2 the results of the Gaussian fits of the different molecular species observed with ALMA towards source A and B, respectively. Table A3 presents the results for the HCO quadruplet observed with the IRAM 30 m telescope.

Table A1. Line parameters measured in the ALMA spectra obtained from Gaussian fits of the different molecular transitions towards IRAS16293−2422 source A.

Molecule	Frequency (GHz)	Transition	Area (K km s^{-1})	Intensity (K)	v_{LSR} (km s^{-1})	FWHM (km s^{-1})
HCO (emission)	86.67076	$1_{0,1} - 0_{0,0}$, J = 3/2–1/2, F = 2–1	5.8 ± 0.8	1.1 ± 0.1	1.9 ± 0.2	4.9 ± 0.6
HCO (absorption)	86.70836	$1_{0,1} - 0_{0,0}$, J = 3/2–1/2, F = 1–0	− 1.3 ± 0.6	− 1.0 ± 0.5	4 ± 1	0.9 ± 0.7
H_2CO	101.33299	$6_{1,5} - 6_{1,6}$	108 ± 4	14.2 ± 0.4	3.14 ± 0.08	7.2 ± 0.2
CH_3OH	86.61560	$7_{2,6} - 6_{3,3}$ − −	182 ± 7	22.2 ± 0.5	3.24 ± 0.08	7.7 ± 0.2
CH_3OH	86.90295	$7_{2,5} - 6_{3,4}$ + +	185 ± 6	22.7 ± 0.5	3.24 ± 0.08	7.7 ± 0.2
CH_3OH	88.59479	$15_{3,13} - 14_{4,10}$ ++	154 ± 9	19.8 ± 0.7	3.1 ± 0.2	7.3 ± 0.3
CH_3OH	88.94009	$15_{3,12} - 14_{4,11}$ − −	166 ± 8	20.5 ± 0.6	3.3 ± 0.2	7.6 ± 0.3
CH_2OHCHO	101.52785	$14_{5,9} - 14_{4,10}$	3.9 ± 0.6	0.68 ± 0.07	2.9 ± 0.3	5.5 ± 0.6

Table A2. Line parameters measured in the ALMA spectra obtained from Gaussian fits of the different molecular transitions towards IRAS16293−2422 source B.

Molecule	Frequency (GHz)	Transition	Area (K km s^{-1})	Intensity (K)	v_{LSR} (km s^{-1})	FWHM (km s^{-1})
HCO (emission)	86.67076	$1_{0,1} - 0_{0,0}$, J = 3/2–1/2, F = 2–1	5 ± 3	2.3 ± 0.8	2.4 ± 0.5	2.3 ± 0.7
HCO (absoprtion)	86.67076	$1_{0,1} - 0_{0,0}$, J = 3/2–1/2, F = 2–1	− 5 ± 2	− 4 ± 1	4 ± 1	1.0 ± 0.7
HCO (absoprtion)	86.70836	$1_{0,1} - 0_{0,0}$, J = 3/2–1/2, F = 1–0	− 3.2 ± 0.8	− 2.2 ± 0.4	4.4 ± 0.1	1.4 ± 0.3
HCO (absoprtion)	86.77746	$1_{0,1} - 0_{0,0}$, J = 1/2–1/2, F = 1–1	− 3.3 ± 0.5	− 2.8 ± 0.3	4.2 ± 0.1	1.1 ± 0.2
H_2CO	101.33299	$6_{1,5} - 6_{1,6}$	54 ± 3	28.4 ± 0.7	2.43 ± 0.03	1.79 ± 0.05
CH_3OH	86.61560	$7_{2,6} - 6_{3,3}$ − −	23 ± 2	13.1 ± 0.7	2.48 ± 0.05	1.64 ± 0.09
CH_3OH	86.90295	$7_{2,5} - 6_{3,4}$ + +	24 ± 3	13.4 ± 0.8	2.49 ± 0.05	1.7 ± 0.1
CH_3OH	88.59479	$15_{3,13} - 14_{4,10}$ ++	22 ± 2	12.6 ± 0.5	2.38 ± 0.03	1.64 ± 0.08
CH_3OH	88.94009	$15_{3,12} - 14_{4,11}$ − −	23 ± 2	12.9 ± 0.5	2.76 ± 0.03	1.66 ± 0.07
CH_2OHCHO	86.60057	$17_{5,2} - 17_{4,13}$	6.2 ± 0.9	3.9 ± 0.4	2.60 ± 0.07	1.5 ± 0.2
CH_2OHCHO	86.86239	$7_{4,3} - 7_{3,4}$	6 ± 1	3.1 ± 0.4	2.7 ± 0.1	1.7 ± 0.3
CH_2OHCHO	86.87650	$20_{4,16} - 20_{3,17}$	2.9 ± 0.7	1.9 ± 0.3	2.58 ± 0.08	1.4 ± 0.3
CH_2OHCHO	88.53041	$8_{4,5} - 8_{3,6}$	2.9 ± 0.7	1.9 ± 0.3	2.58 ± 0.08	1.4 ± 0.3
CH_2OHCHO	88.69126	$12_{3,10} - 12_{2,11}$	6 ± 2	3.7 ± 0.6	2.8 ± 0.1	1.4 ± 0.3
CH_2OHCHO	88.89245	$9_{4,6} - 9_{3,7}$	5 ± 1	3.4 ± 0.5	2.82 ± 0.08	1.4 ± 0.2
CH_2OHCHO	99.06847	$14_{4,11} - 14_{3,12}$	6 ± 2	5.1 ± 0.7	2.61 ± 0.07	1.2 ± 0.2
CH_2OHCHO	101.11631	$21_{4,17} - 21_{3,18}$	7 ± 2	4.3 ± 0.7	2.5 ± 0.2	1.6 ± 0.3
CH_2OHCHO	101.21981	$18_{3,15} - 18_{2,16}$	1.5 ± 0.4	0.9 ± 0.2	2.67 ± 0.09	1.6 ± 0.2
CH_2OHCHO	101.23217	$15_{2,13} - 15_{1,14}$	6 ± 2	3.8 ± 0.6	2.6 ± 0.2	1.5 ± 0.3
CH_2OHCHO	101.51469	$14_{3,12} - 14_{2,13}$	1.3 ± 0.5	0.6 ± 0.2	2.3 ± 0.2	1.9 ± 0.5
CH_2OHCHO	101.52785	$14_{5,9} - 14_{4,10}$	7.6 ± 0.9	4.1 ± 0.3	2.53 ± 0.06	1.7 ± 0.2

Table A3. HCO line parameters measured in the IRAM 30 m spectra obtained from Gaussian fits.

Molecule	Frequency (GHz)	Transition	Area (K km s^{-1})	Intensity (K)	v_{LSR} (km s^{-1})	FWHM (km s^{-1})
HCO	86.67076	$1_{0,1} - 0_{0,0}$, J = 3/2–1/2, F = 2–1	0.07 ± 0.04	0.03 ± 0.01	3.6 ± 0.4	2.0 ± 0.7
HCO	86.70836	$1_{0,1} - 0_{0,0}$, J = 3/2–1/2, F = 1–0	0.06 ± 0.03	0.03 ± 0.01	4.2 ± 0.4	1.8 ± 0.6
HCO	86.77746	$1_{0,1} - 0_{0,0}$, J = 1/2–1/2, F = 1–1	0.03 ± 0.02	0.016 ± 0.008	4.3 ± 0.5	1.6 ± 0.8
HCO	86.80578	$1_{0,1} - 0_{0,0}$, J = 1/2–1/2, F = 0–1	0.03 ± 0.02	0.02 ± 0.01	4.4 ± 0.5	1.1 ± 0.9

APPENDIX B: FIT OF THE CONTINUUM LEVEL

To reproduce the continuum level of the spectra, we have used a modified blackbody function:

$$T_c(\nu) = f_c(\nu) B_\nu(T_c)(1 - e^{-\tau(\nu)}) = f_c(\nu) \frac{h\nu}{k} \frac{1}{e^{h\nu/kT_c} - 1}(1 - e^{-\tau(\nu)}), \quad \text{(B1)}$$

where $B(T_c)$ is the blackbody function with temperature T_c, $f_c(\nu)$ is the beam filling factor of the continuum emission in each spectral window, and $\tau_d(\nu) = \tau_{d0}(\nu/\nu_0)^\beta$ is the dust optical depth, where β is the dust emissivity spectral index. We adopted $\nu_0 = 94$ GHz (the intermediate frequency of the four spectral windows) and assumed that T_c is equal to the excitation temperature derived from CH_3OH, 178 K and 181 K for sources A and B respectively (see Section 3.2.3). To calculate the beam filling factor we used the synthesized beams of the data cubes of the different spectral windows (Table 1) and the deconvolved sizes of the continuum sources of A and B at 94 GHz (Fig. 1): 1.1 × 0.7 and 0.46 × 0.42 arcsec, respectively.

We fitted the continuum emission of both hot corinos in all spectral windows by varying the values of β and τ_{d0}. The dust emissivity spectral index β reflects the dependence of the continuum emission with the frequency, i.e. the t of the continuum emission, while the dust optical depth τ_{d0} controls the level of the continuum emission. We tried multiple combinations of both parameters (some examples are shown in Figs B1 and B2) and chose by visual inspection the solutions that fit better the continuum level of the four spectral windows in each hot corino. Although the determination of the continuum level is not univocal due to the presence of multiple lines in such a crowded spectra, we note that the uncertainty from the visual inspection is lower than the rms of the spectra and the uncertainty of the flux calibration, which we used to derive the errors of τ_{d0} and β. The fits that better reproduce the continuum level in all spectral windows are $\beta = 0.9$ and $\tau_{d0} = 0.09$ for source A and $\beta = 0$ and $\tau_{d0} = 2.1$ for source B (see Figs B1 and B2). We used these parameters to fit the continuum level in Section 3.1.

We assumed a flux density calibration error of ±5 per cent, from Jørgensen et al. (2016) and Bonato et al. (2018). According to this, we expect calibration uncertainties of around ±0.3 and ±1 K for source A and B, respectively. We added to these values the rms of the spectra (0.15 and 0.18 K, respectively), obtaining a total uncertainty in the continuum fluxes of ±0.45 and ±1.18 K, respectively. Considering this, the values of τ_{d0} with their associated uncertainties are $0.09^{+0.01}_{-0.01}$ and $2.1^{+0.6}_{-0.4}$ for source A and B, respectively. To estimate the error of β we only considered the rms of the spectra and not the calibration uncertainty, since β is giving the behaviour with frequency and the calibration of the four spectral windows was the same. We then obtained for β: 0.9 ± 0.4 and 0.0 ± 0.5 for source A and B, respectively.

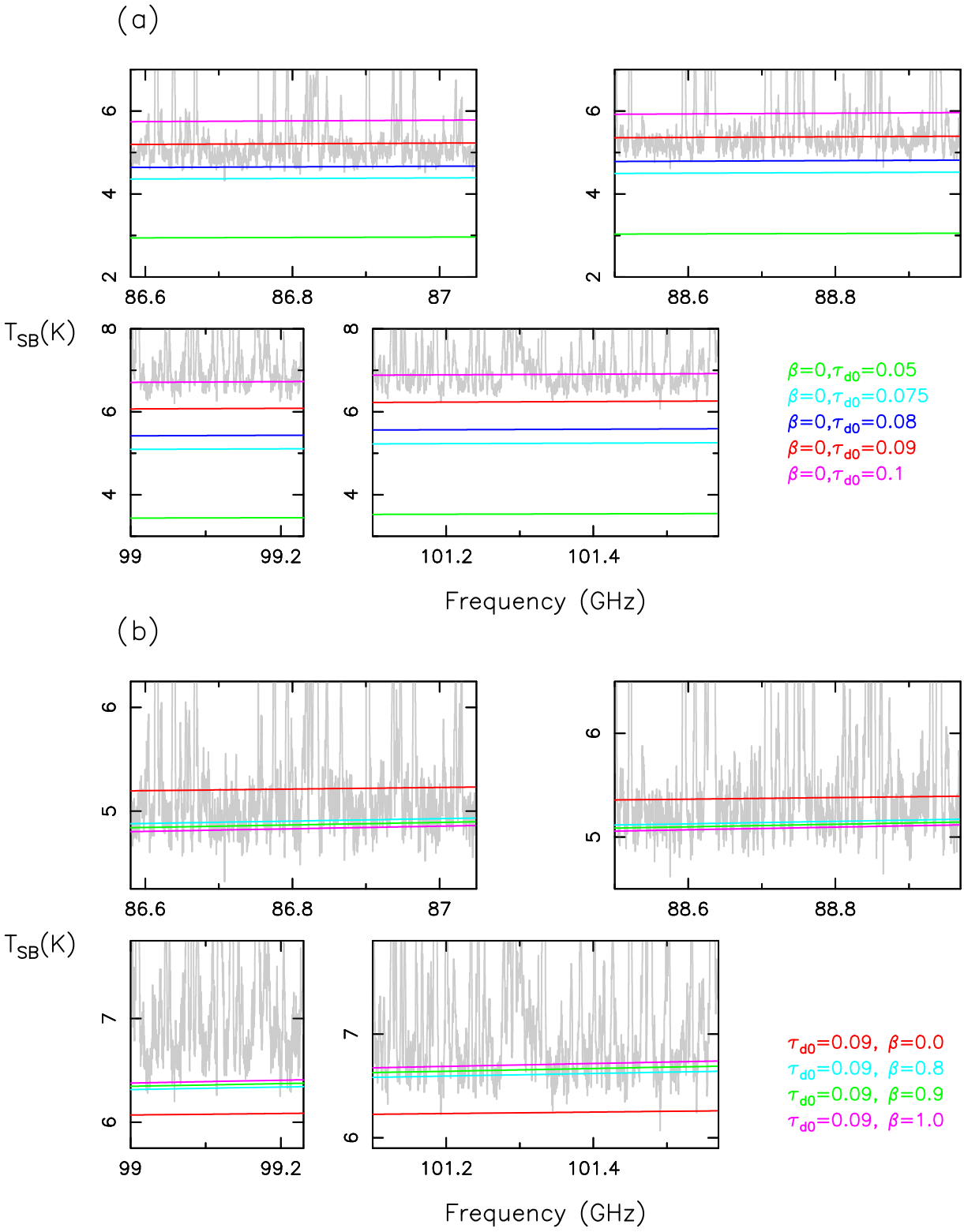

Figure B1. Fit of the continuum level in the spectra towards the continuum peak of IRAS16293 A. The four different spectral windows are shown. The coloured lines show different fits with different pairs of values of τ_{d0} and β. We adopted $\nu_0 = 94$ GHz and $T_c = 178$ K. To calculate f_c we used a size of 1.1 × 0.7 arcsec. *Panel (a)*: We show different fits keeping $\beta = 0$ and varying the value of τ_{d0}. *Panel (b)*: We show different fits keeping $\tau_{d0} = 0.09$ and varying the value of τ_{d0}.

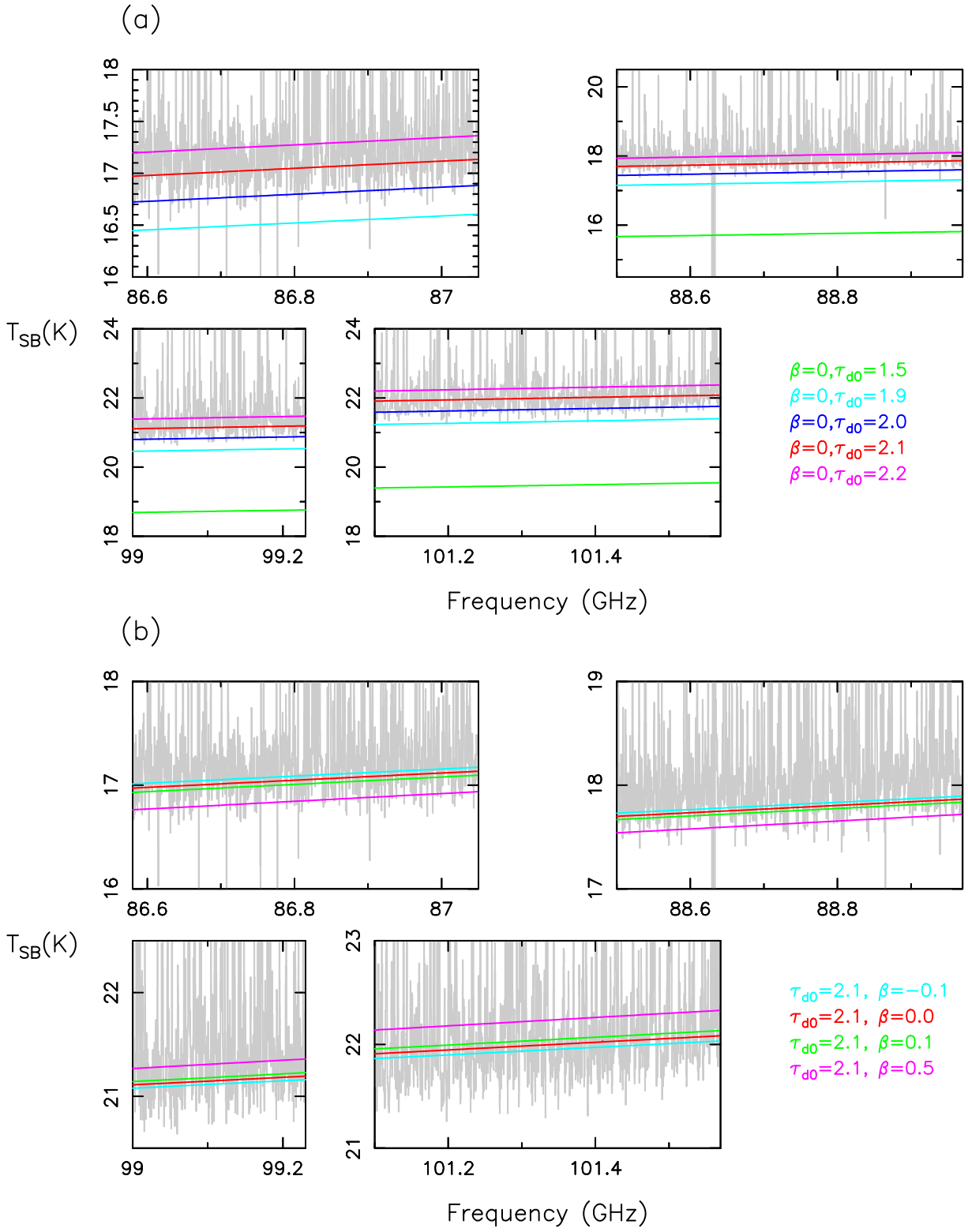

Figure B2. Fit of the continuum level in the spectra towards the continuum peak of IRAS16293 B. The four different spectral windows are shown. The coloured lines show different fits with different pairs of values of τ_{d0} and β. We adopted $\nu_0 = 94$ GHz and $T_c = 181$ K. To calculate f_c we used a size of 0.46×0.42 arcsec. *Panel (a)*: We show different fits keeping $\beta = 0$ and varying the value of τ_{d0}. *Panel (b)*: We show different fits keeping $\tau_{d0} = 2.1$ and varying the value of τ_{d0}.

This paper has been typeset from a TEX/LATEX file prepared by the author.